ETH
Eidgenössische Technische Hochschule Zürich
Swiss Federal Institute of Technology Zurich

PAUL SCHERRER INSTITUT
PSI

Single Beam Wollaston Interferometry of a Gas Jet with non-Uniform Density towards Laser Wakefield Acceleration

Master Thesis

Department of Physics
ETH Zurich

Author

BSc ETH Physics
Benedikt Hermann

Supervisor

Dr. Andreas Adelmann

Scientific Advisor

Dr. Rasmus Ischebeck

March 13, 2017

Eidgenössische Technische Hochschule Zürich
Swiss Federal Institute of Technology Zurich

Declaration of originality

The signed declaration of originality is a component of every semester paper, Bachelor's thesis, Master's thesis and any other degree paper undertaken during the course of studies, including the respective electronic versions.

Lecturers may also require a declaration of originality for other written papers compiled for their courses.

I hereby confirm that I am the sole author of the written work here enclosed and that I have compiled it in my own words. Parts excepted are corrections of form and content by the supervisor.

Title of work (in block letters):

Single Beam Wollaston Interferometry of a Gas Jet with non-Uniform Density towards Laser Wakefield Acceleration

Authored by (in block letters): *For papers written by groups the names of all authors are required.*

Name(s):	**First name(s):**
Hermann	**Benedikt**

With my signature I confirm that

- I have committed none of the forms of plagiarism described in the 'Citation etiquette' information sheet.
- I have documented all methods, data and processes truthfully.
- I have not manipulated any data.
- I have mentioned all persons who were significant facilitators of the work.

I am aware that the work may be screened electronically for plagiarism.

Place, date	**Signature(s)**
Zurich, March 12, 2017	

For papers written by groups the names of all authors are required. Their signatures collectively guarantee the entire content of the written paper.

Abstract

This master's thesis examines two different supersonic gas jets operating with Argon by a single beam interferometer based on a Wollaston prism. The closing mechanism of the first valve uses the piezoelectric force which enables short (7 µs) opening times at repetition rates of several kHz. This type of gas jet is used for an electron bunch length monitor at the free electron laser at Paul Scherrer Institute (SwissFEL, PSI). The second valve to be studied is a solenoid valve, which can sustain higher backing pressures and can therefore provide higher Argon densities (at 35 bar, 1 mm close to the nozzle: $1 \times 10^{19}\,\mathrm{Ar/cm^3}$). For the purpose of Laser Wakefield Acceleration (LWFA) in the linear regime such high densities as well as a density down ramp are needed for electron injection. Hence, a supersonic shock front arising from a razor blade inserted laterally to the gas flow is investigated via tomography. Finally, first LWFA experiments are carried out with the Aramis Seedlaser facility (Ti:Sa, 35 mJ) at PSI. Measurements with a Faraday cup show a strong dependency of the accelerated charge (several fC) on the Argon density. Detailed studies on the electron bunch will be carried out with an energy spectrometer in a further master's thesis.

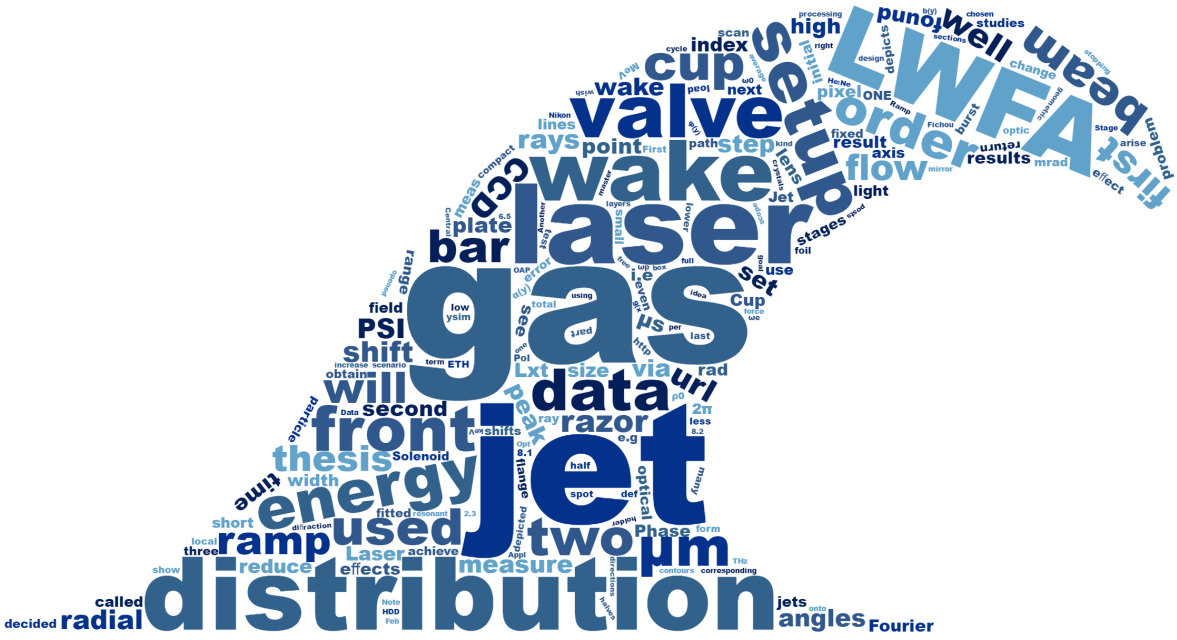

Frequently used terms

Contents

1 Introduction **3**

2 Theory of Wollaston Interferometry and Gas Jets **5**
2.1 Wollaston Prism 5
2.2 Estimation of Phase Shift due to a Gas Jet 6

3 Experimental Setup for Gas Density Measurements **9**
3.1 Wollaston Interferometer 9
3.2 Tomography 10
3.2.1 Eccentricity Correction 12

4 Data Analysis for Interferometry and Tomography **15**
4.1 Phase Unwrapping based on a Discrete Fourier Transform 15
4.2 Abel Inversion 17
4.3 Tomographic Reconstruction 18
4.3.1 Back Projection 18
4.3.2 Maximum Likelihood – Expectation Maximisation (ML–EM) 18
4.3.3 Convergence and Error Studies of ML–EM 21

5 Density Measurements **23**
5.1 Piezo Valve 23
5.2 Solenoid Valve 25
5.3 Shock Front Characterization 25
5.4 Error and Stability Analysis 27

6 Laser Wakefield Acceleration **31**
6.1 Setup for Focusing and Positioning the Ti:Sa Laser 31
6.2 Faraday Cup 34
6.3 First LWFA Experiments 37

7 Summary and Outlook **40**

8 Appendix **42**
8.1 Assembly of Rotational Setup 42
8.2 IOTA ONE Solenoid Valve Controller 42
8.3 Faraday Cup Design 46
8.4 Python Functions 46
8.5 List of Main Devices 48

Chapter 1

Introduction

Accelerated particles are applied in a wide variety of disciplines, for instance collider physics, diffraction experiments, cancer treatment, medical imaging, electron microscopy and many more. A problem that often arises is the size of these machines. LHC at CERN with a circumference of nearly 30 km, for example, is among the largest and most expensive experiments in our society. Yet in hospitals, small accelerators for cancer treatment are advantageous. Advanced accelerator science tries to build accelerating structures that sustain a higher electric field gradient to downsize the structure compared to conventional microwave cavities. Laser wakefield acceleration (LWFA) is one such promising technology which is being investigated by several research groups around the world [1, 2, 3]. The idea of LWFA is to resonantly excite a wake field in a plasma by a short energetic laser pulse. The plasma can be created in advance by another source or can be generated by ionization of the wake–generating pulse itself. An electron is trapped and accelerated depending on its phase, i.e. its position and velocity with respect to the wake. An injection method without timing issues is self–injection by a density down–ramp. Consider a wake which is generated in two preceding regions with different density. The electrons from the higher density region oscillate faster as the plasma frequency ω_p depends on the electron density n_e:

$$\omega_p = \sqrt{4\pi n_e e^2/m}, \tag{1.1}$$

where m and e are mass and charge of the electron. Some of the fast oscillating electrons from the first region will be trapped in the accelerating phase of the plasma wake of the second region with lower density [4]. In other words, the wave breaks due to a density variation. It has been shown, that a density change by a factor of 2 to 3 can be achieved by a shock front in supersonic gas jets [5]. It is desirable that the density variation happens within a short distance in order to inject many electrons simultaneously, which will result in a narrow energy spread of the accelerated electrons. In the present master's thesis I also examine the feasibility of LWFA with a laser facility at PSI (Aramis Seedlaser, 800 nm, 20 fs, 35 mJ). The density down–ramp for injection is created by a razor blade inserted to a supersonic Argon gas flow. For this purpose, the density distribution has to be measured and optimized. The density is studied with a Wollaston interferometer for different backing pressures and blade positions. Another critical task is to focus the wake driving Ti:Sa laser

pulse down to a sub–10 µm focal spot into the density ramp of the gas jet, in order to achieve a sufficient electric field for ionizing the gas and generating the plasma wake. The LWFA experiment is supposed to be a platform for students to develop an understanding of advanced acceleration concepts within the scope of the advanced physics lab at ETH Zurich, semester or master theses. Possible topics might include interferometry of gas jets, image reconstruction, laser acceleration, electron beam characterization or even diffraction experiments with the extracted electron beam. Nick Sauerwein has recently started to work on beam optimization and characterization with a permanent magnet spectroscope as his master's thesis. Further activities using the accelerated electron bunch from this setup are in the planning stage. For instance, the ACHIP (acceleration on a chip) collaboration may perform acceleration experiments with a dielectric structures and THz laser fields.

Chapter 2

Theory of Wollaston Interferometry and Gas Jets

This chapter describes the working principles of the Wollaston interferometer and provides estimates for phase shifts arising from gas jets.

2.1 Wollaston Prism

A Wollaston prism (Figure 2.1b) consists of two crystals (e.g. quartz) which have a single optic axis. The axes of the two halves are rotated by 90 degrees. The main feature of such crystals is that the refraction index for light polarized parallel (n_e) to the optic axis is larger than for light polarized perpendicular (n_o) to the optic axis. Hence, a light ray polarized at 45° with respect to the optic axis is split up in two equally intense beams which have perpendicular polarization. The two rays will leave the prism at an angle ϵ (dispersion angle), which depends on the geometric and optical properties of the crystals forming the Wollaston prism. As exposed by Small [6],

$$\epsilon = 2\beta(n_e - n_o), \tag{2.1}$$

where β is the angle between the two halves of the prism (see Figure 2.1a). The Wollaston prism used in this experiment manufactured by Societe d'Optique de Precision Fichou (Figure 2.1b) has a dispersion angle of $20'' = 5.8$ mrad. If two light rays with initial relative angle ϵ pass through the prism, the orthogonal part of the first ray will coincide with the perpendicular part of the second ray (compare Figure 2.1a). Before passing through the lens these two rays are separated by a distance $d = \epsilon f$. For the used Wollaston prism and a lens with focal length f of 30 cm d is equal to 1.74 mm. If a second polarizer at $-45°$ is placed after the prism, these two rays can interfere. This concept is illustrated in Figure 2.1a. Depending on the position of the prism relative to the focal point of the lens the interfering rays will pick up a phase difference. If the prism is centered at the focal point, every optical path runs equal distances through the two halves of the prism, i.e. no relative phase difference is generated. This scenario is called normal mode or infinite fringe width

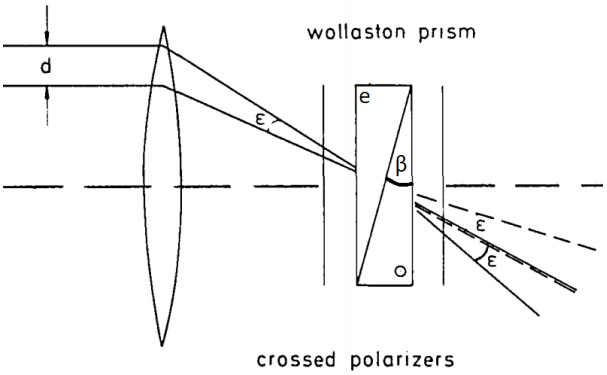

(a) Working principle of the Wollaston prism, taken from [9].

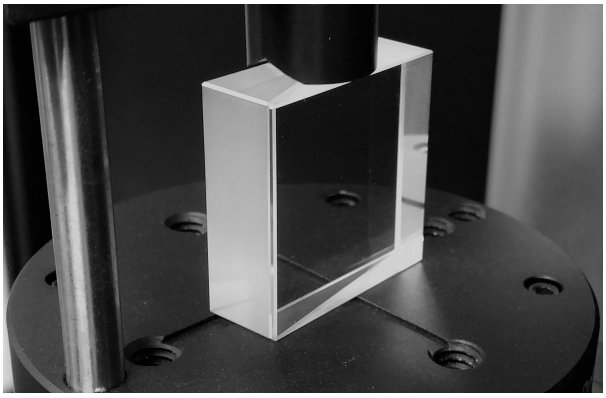

(b) Wollaston prism 30x30x5 mm, $\epsilon = 5.8$ mrad, Societe d'Optique de Precision Fichou.

Figure 2.1

(IFW) setup. Displacing the prism by a distance b from the focal point results in different path lengths of interfering rays, as they travel different distances in each half of the prism. These phase shifts lead to regular interference patterns on the screen. This setup ($b \neq 0$) is called differential mode or finite fringe width (FFW) setup [7]. The FFW setup is sketched in Figure 3.1. The spacing S between the undisturbed fringes is:

$$S = \frac{\lambda}{\epsilon}\frac{p}{b}, \tag{2.2}$$

where p is the distance of the screen from the focal point of the lens [8]. The spacing can be decreased by increasing b, the position of the Wollaston prism. If the screen is hold fix, p changes accordingly. Placing a medium with refractive index $n \neq 1$ that covers only parts of the laser beam will result in a shift of the fringe spacing S, since rays passing through the medium will pick up an additional phase shift with respect to unperturbed rays.

2.2 Estimation of Phase Shift due to a Gas Jet

A local density gradient imposes a varying refractive index n, resulting in a phase shift $\Delta\phi$ of rays passing through that particular region. Therefore, the undisturbed fringe spacing is locally shifted by ΔS. The relationship between the atom density ρ and refractive index n of a gas is given by the Lorentz–Lorenz equation [10]:

$$\rho = \frac{n^2 - 1}{n^2 + 2}\frac{N_A}{A} \approx (n-1)\frac{2}{3}\frac{N_A}{A}, \tag{2.3}$$

where N_A is Avogadro's number and A is the molar refractivity, e. g. $A_{Ar} \approx 4.20 \times 10^{-6}$ m^3/mol. The approximation is valid for $n \approx 1$, which is true for a gas with densities

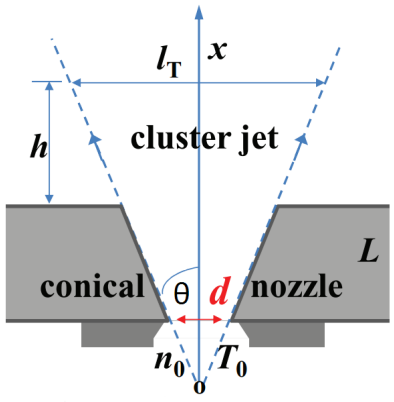

Figure 2.2: Sketch of a conical nozzle, taken from [11]. Parker solenoid valve: $d = 500\,\mu m$, $L = 250\,\mu m$, $\theta = 45°$.

below 10^{19} particles per cm^3. Inverting equation 2.3 yields the dependency of the refractive index on the density. Assuming a homogeneous density within a gas jet of diameter l, the generated phase shift between interfering rays in the linear approximation (equation 2.3) is:

$$\Delta\phi \approx l(n-1)\frac{2\pi}{\lambda} = l\frac{3\pi}{\lambda}\frac{A}{N_A}\rho. \tag{2.4}$$

This expression yields an upper limit for the phase shift, since the used gas jet has a circular throat and hence, produces a cylindrically symmetric gas flow, i.e. the length of a path through the gas is at most l. As described above, the fringe spacing is affected by the phase shift in the FFW setup; the fractional fringe distance shift is given by:

$$\frac{\Delta S}{S} = \frac{\Delta\phi}{2\pi}. \tag{2.5}$$

Next, the gas density when using the solenoid valve (Parker Miniature High–Speed Valve) is estimated. The pressure of the gas before leaving the nozzle, called backing pressure P_b, as well as the nozzle design play a crucial role for the density of the jet. The gas jet used in the present experiment allows for backing pressures up to 80 bar and has a conical nozzle with an half opening angle $\theta = 45°$ (see Figure 2.2). As described by Chen [11] the on–axis particle density at position x of a conical gas jet is approximately given by

$$\frac{\rho}{\rho_0} = 0.15\left(\frac{0.74d}{x\tan\theta}\right)^2, \tag{2.6}$$

where x is defined as depicted in Figure 2.2, ρ_0 is the atom density of the gas before leaving the nozzle and d is the throat diameter of the valve. The gas jet used in this study has a throat diameter of 500 µm and L is 250 µm. Using the ideal gas law which is a good assumption for Argon and Xenon at room temperature, ρ_0 is determined by the backing pressure P_b which

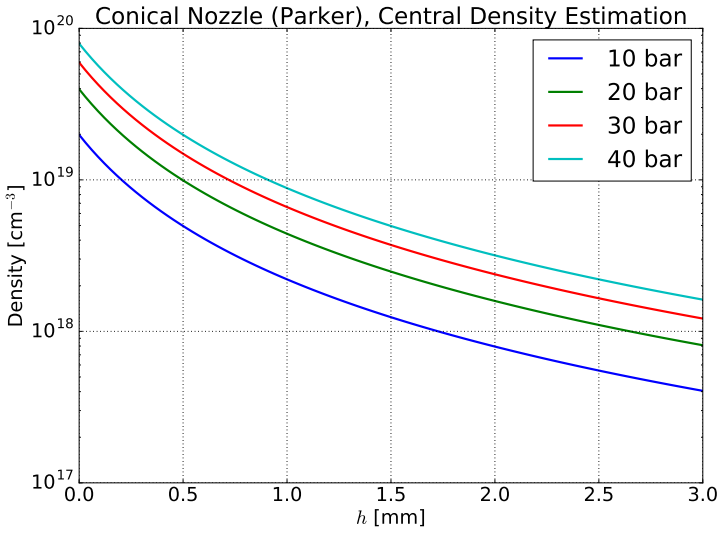

Figure 2.3: Estimation of the on–axis density ρ for different backing pressures. This model is based on the ideal gas law, i.e. independent of the gas species.

refers to the pressure in the chamber before the nozzle as well as the temperature of the nozzle T_0 via: $\rho_0 = P_b/(k_B T_0)$ where k_B is the Boltzmann constant. Figure 2.3 shows the on–axis density n with respect to h (distance from the end of the nozzle) for different backing pressures from 10 to 40 bar for the dimensions of the Parker solenoid valve. To excite the plasma wake resonantly with a 15 femtosecond laser pulse an Argon density in the order of $1.75 \times 10^{18}\,\mathrm{cm}^{-3}$ is needed [4]. The required density at $h = 2.5$ mm (distance from the nozzle) is achieved with backing pressures of around 30 bar. According to equation 2.4 the phase shift of a gas jet with an average density ranging from $1 \times 10^{18}\,\mathrm{cm}^{-3}$ to $1 \times 10^{19}\,\mathrm{cm}^{-3}$ lies between 0.1 rad and 1 rad. A phase shift of this order is expected to result in a clearly visible change of the interference pattern described by equation 2.5.

Chapter 3

Experimental Setup for Gas Density Measurements

The Wollaston interferometer to measure the gas density is set up on a single breadbord (75 cm×125 cm), such that the optical setup and vacuum chamber with the gas jet forms a compact unit that can be transported without much reassembly. In the next sections the details of the optical setup as well as the setup for tomography of a non–symmetric density distribution are explained.

3.1 Wollaston Interferometer

In Section 2.1 the theory of the Wollaston prism interferometer is exposed. This section presents the experimental realization of the interferometer, which is depicted in Figure 3.1 and Figure 3.2. A linearly polarized continuous He:Ne laser with a wavelength λ_I of 632.8 nm and an output power of 21 mW is used as a coherent light source for the interferometer. To prevent upstreaming air due to the heat of the laser from causing unwanted phase shifts the laser is placed outside of the black cardboard box that contains the interferometer. The box also reduces noise as it minimizes the airflow in the whole experiment, as well as external photons hitting the CCD sensor. The mutual laser diameter is 0.7 mm ($1/e^2$ width). The telescope (20x) attached to the laser provides a beam with a diameter of 14 mm, which is suitable to study a gas jet of a few millimeter. The noise of the acquired images is expected to be lowest in the center of the beam due to the higher intensity of the laser in that region. The vacuum chamber has two facing broadband–anti–reflective windows for the He:Ne interferometer laser to pass the gas jet. The gas jet is mounted on the top of the vacuum chamber. The gas flows downwards towards the vacuum pump (Pfeiffer HiCube Eco 300, 300 L s^{-1}). The Parker solenoid valve is operated at 0.5 to 3 Hertz and with opening times T less than 12 ms to reduce the gas load on the pump. The Wollaston prism is placed between two crossed polarizers, such that the interference fringes are parallel to the jet. The interference pattern is captured with a CCD camera (Basler, aviator avA2300–25gm) and a f = 200 mm Nikon camera lens. The minimal exposure time of the camera is 18 µs. The

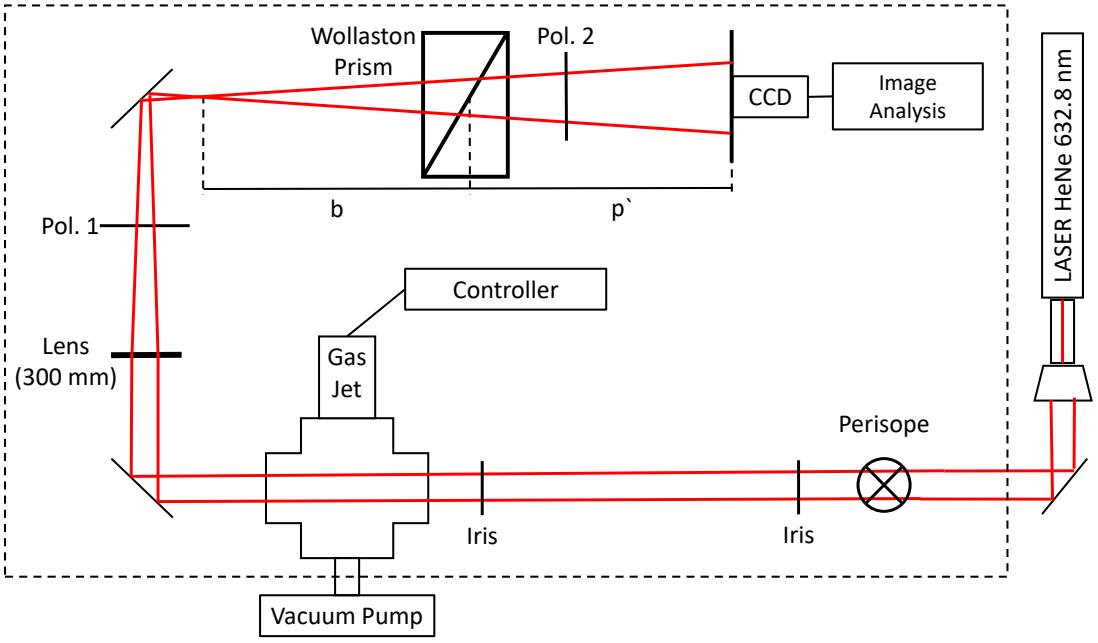

Figure 3.1: Sketch of the setup for Wollaston interferometry. The dashed line represents the breadboard with the shielding box around it. The Wollaston prism is mounted on a linear stage, such that the parameter b and therefore the fringe spacing S can be changed (see section 2.1). A f = 200 mm Nikon imaging lens is attached to the CCD camera.

exposure time is set to 30 µs in order to obtain an image with good contrast without reaching saturation of the sensor. The timing of the camera is as follows: the reference image (I1) is recorded 50 ms before the trigger signal T1 is sent to the solenoid controller. The second image I2 is recorded 2 ms after signal T1 such that the valve is completely opened during the total acquisition time. Further Reduction of the time between I1 and T1 (50 ms) causes read out issues of the camera. Figure 3.3b shows a typical interference pattern of the undisturbed gas jet. The change of the fringe distance due to the gas distribution is clearly observable when the Parker solenoid valve is operated at 35 bar backing pressure. The data processing for the obtained interference fringes is explained in section 4.1.

3.2 Tomography

The Wollaston interferometry setup exposed in the previous section can be used to measure phase projections along the propagation direction of the interferometry laser (He:Ne). An optically transmitting object that has a refractive index close to 1 (e. g. a gas jet) can be characterized. If the studied object can be assumed to be rotationally symmetric, Abel inversion (section 4.2) yields the 3D density distribution from a single phase projection. To

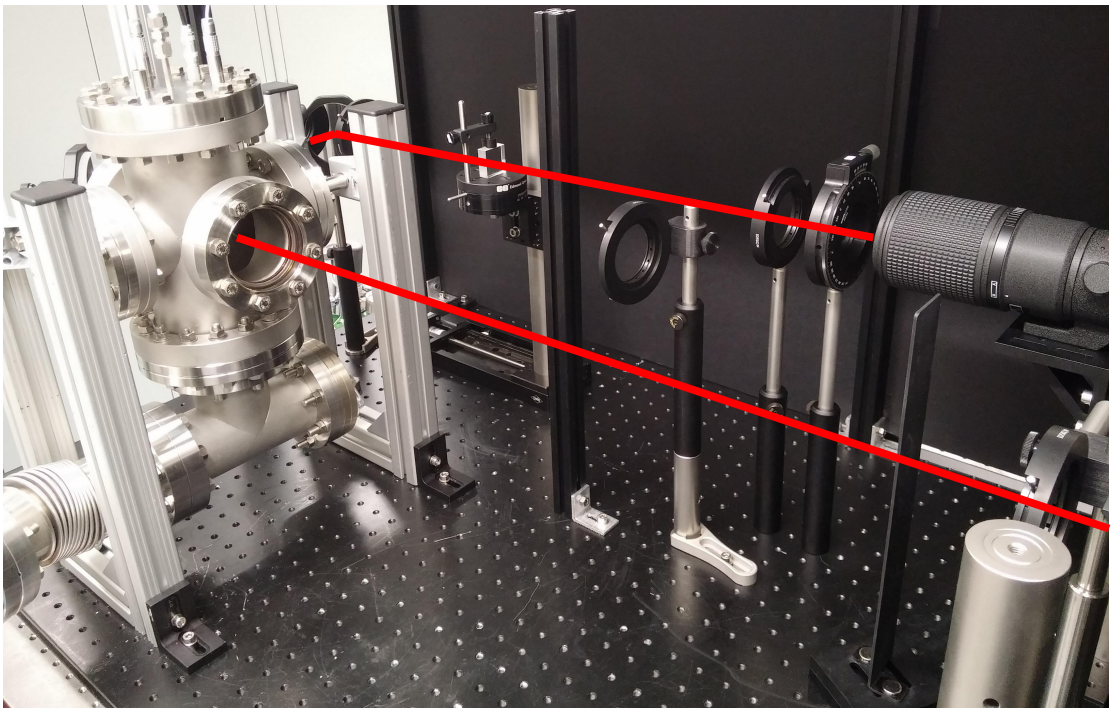

Figure 3.2: Experimental setup for Wollaston interferometry. The expanded beam passes through the gas jet, the first polarizer, lens, Wollaston prism, second polarizer and is projected onto the CCD screen via a 200 mm imaging lens (AF Micro–Nikkor 200 mm f/4D IF–ED, Nikon).

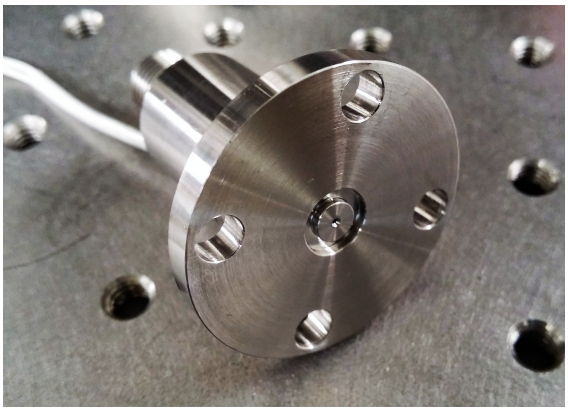

(a) Miniature high speed high vacuum dispense valve with conical outlet (Parker 009–0442–900).

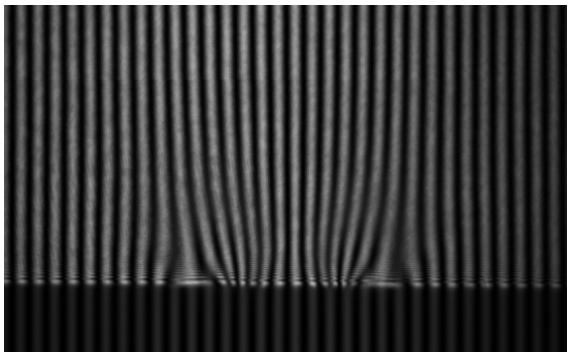

(b) Typical interference fringes of Parker solenoid valve at 35 bar backing pressure with Argon. In this image the gas flow is directed upwards.

Figure 3.3

obtain the 3D density distribution of a non–rotational symmetric object (e. g. gas jet with shock front) several projections along different angles are needed. The 3D distribution can be reconstructed with tomographic algorithms, for instance Maximum Likelihood Expectation Maximization (ML–EM), which is explained in section 4.3.2. Here, the experimental setup to obtain tomographic projection data of the solenoid gas jet with a supersonic shock front arising from a razor blade is described. The idea is to position the blade around the gas jet with two degrees of freedom. This is achieved with a rotational piezo stage (Smaract, SR–5714C–S) and a linear piezo positioner (Smaract, SLC–1720–S) which is attached to the rotational stage. The rotational stage is used to measure phase projections along different directions. The radial position can be used to vary the position of the blade with respect to the gas jet. This enables to control properties of the shock front. Furthermore, the radial degree of freedom is used to correct the eccentricity between the gas jet and the rotational stage due to mechanical imperfections. The distance between razor blade and nozzle of the gas jet is fixed in this setup (1.6 mm). Figure 3.4 depicts the rotation module for tomography. The CF 100 flange has feed–throughs for gas, valve control and Smaract motor controls (3x). The gas jet is centered onto the flange and the rotational stage is mounted with 3 custom–made posts and an adapter plate. The linear stage is connected to the rotational stage with a second adapter plate. This adapter plate has a centered hole with a diameter 0.5 mm larger than the diameter of the gas jet in order to achieve an eccentricity smaller than 250 µm. If the space between the jet and the plate is too small, the rotational stage will be blocked easily due to friction. This happens also when the jet is not mounted carefully, i. e. parallel to the flange. Finer centering is achieved with the procedure explained in section 3.2.1, which basically corrects the radial position according to the measured eccentricity. To avoid blocking of the rotational stage, the hole in the plate could be enlarged. The razor blade is glued to a u–shaped aluminum holder (Figure 8.1) which is screwed to the linear positioner. Detailed instructions about the components and for rebuilding the module can be found in the appendix (8.1).

3.2.1 Eccentricity Correction

The center of the gas jet and the center of the rotation of the blade may not coincide due to mechanical imperfections. From phase projections of the shock wave with a fixed blade, expected density gradients are on a length scale of tens of µm. It would be a difficult task to position the gas jet in the center of the stage with sub 10 µm precision. Therefore, it is decided to measure the eccentricity between jet and blade with a microscope (2x magnification) and a CCD camera (Basler, scout scA1400–17gm) to obtain a correction factor for the radial position with respect to the angular position. The eccentricity is calculated by fitting a line to the edge of the blade for 13 angular positions ranging from 0° to 180° (15° step width). The center of a circle with the fitted lines as tangents provides the eccentricity. The center can be found by defining an adequate optimization function. The following minimization problem turned out to converge quickly to the solution. The center is the point that is equal–distant to all tangents. Therefore, minimizing the standard deviation of the set of the center to tangent distances yields the center of the blade. This optimization problem is solved with

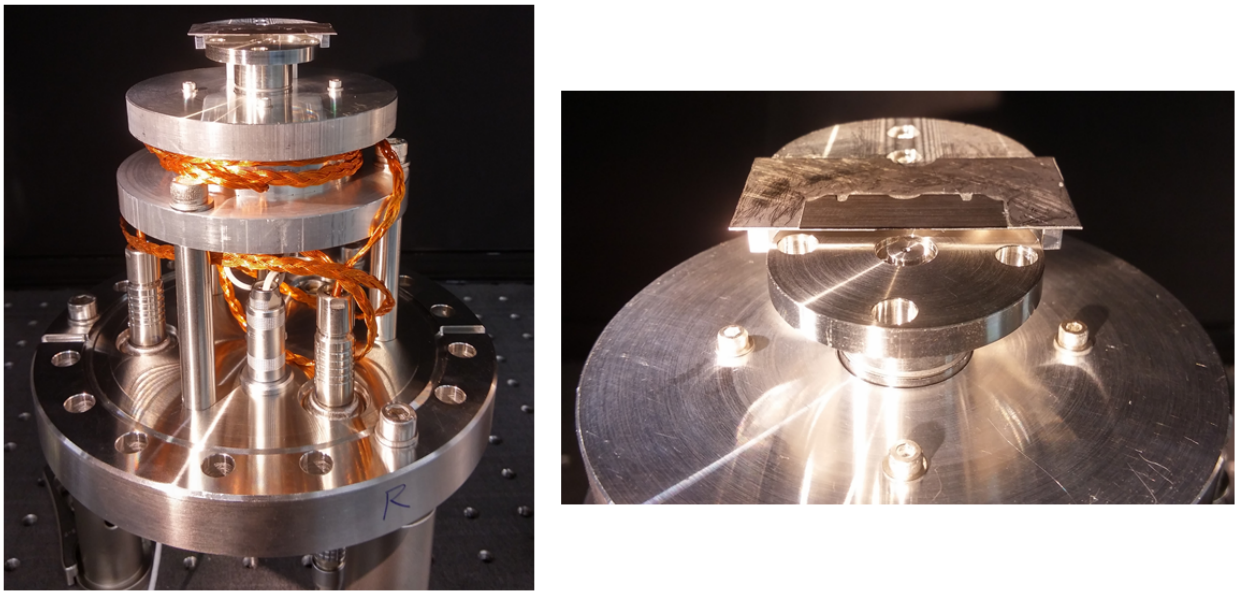

Figure 3.4: Tomography setup for shock front studies. A razor blade is positioned with linear and rotational stages manufactured by Smaract (SR–5714C–S and SLC–1720–S).

the `scipy.optimize.minimize` routine. Consider the following coordinate system. The center of the gas jet is at the origin and the eccentricity (fitted center of rotation) is named $\vec{E} = (E_1, E_2)$. Let θ be the angle of the rotation starting on the E_1–axis (see Figure 3.5). Then, the resulting radial offset of the blade at angular position θ is given by:

$$r_{\text{diff}}(\theta) = E_1 \cos(\theta) + E_2 \sin(\theta). \tag{3.1}$$

This formula yields the radial correction factor r_{diff} that is needed to correct for the eccentricity between gas jet and blade. Figure 3.6 shows images taken by the microscope of the uncorrected blade position at three different angles. The fitted center of the blade overlays these images. The eccentricity is easily visible by eye. Figure 3.7 shows the blade positions after correcting for the eccentricity with the previously explained optimization. The expected reduction of the eccentricity is clearly observed. The eccentricity is reduced from 200 µm to 10 µm, which is sufficient to study density gradients on a length scale of tens of µm.

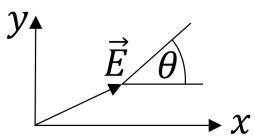

Figure 3.5: Coordinates for eccentricity correction.

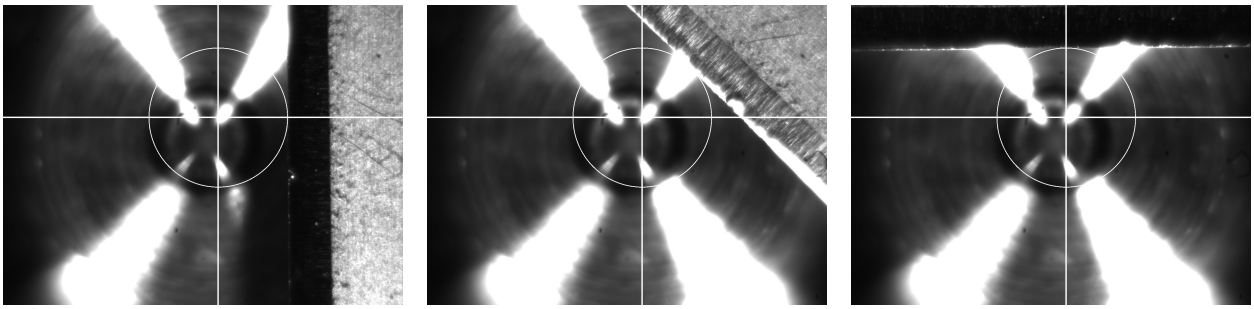

(a) 0° (b) 45° (c) 90°

Figure 3.6: Position and center of blade rotation before eccentricity correction.

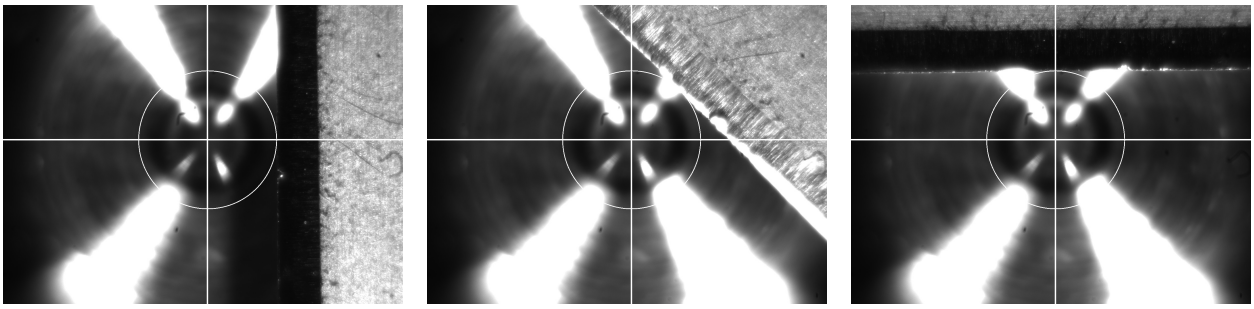

(a) 0° (b) 45° (c) 90°

Figure 3.7: Position and center of blade rotation after eccentricity correction.

Chapter 4

Data Analysis for Interferometry and Tomography

The interference fringe images obtained by the Wollaston interferometer (section 3.1) need to be evaluated numerically to obtain quantitative information about the phase projections. This as well as methods to reconstruct the spatial density distribution of rotationally symmetric as well as non–symmetric distributions are exposed in this chapter.

4.1 Phase Unwrapping based on a Discrete Fourier Transform

The undisturbed fringes are mathematically described by a harmonic oscillation with fixed frequency multiplied by the Gaussian amplitude of the He:Ne laser beam profile. The wave period of the oscillation is given by the undisturbed fringe width S (equation 2.2). A gas jet will locally change the fringe width according to its phase. The following phase extraction problem arises. Given noisy discrete values of a function of the form:

$$g(y) = b(y) \cdot e^{\mathrm{i}[2\pi f y + \alpha(y)]}, \tag{4.1}$$

where $\alpha(y)$ represents the phase shift induced by the gas jet. The term $b(y)$ takes global intensity changes due to the Gaussian profile of the interferometry laser into account, y is the coordinate perpendicular to the gas flow and interferometry laser and f is the oscillation frequency of the undisturbed fringes. This problem can be solved by fitting the measured data to an Ansatz for $\alpha(y)$. This is not appropriate, since one has to make (possibly incorrect) assumptions about the form of $\alpha(y)$. Especially, when a shock front has to be characterised by $\alpha(y)$. A more elegant way to directly unwrap the phase from the noisy data makes use of Fourier Transform.

- **Fourier Transformation of g**

$$\mathcal{F}(g)(\omega) = \int_{-\infty}^{+\infty} e^{-\mathrm{i}2\pi\omega y} \cdot b(y) \cdot e^{\mathrm{i}[2\pi f y + \alpha(y)]} \, \mathrm{d}y \tag{4.2}$$

Since the acquired signal is real, the whole information is contained in the positive frequency domain where the spectrum has two significant peaks. One at the fringe frequency f and another at zero due to the slowly varying Gaussian intensity profile of the beam. A Gaussian window is applied to the spectrum to cut this peak.

- **Rotation of the Fourier–transformed signal**

$$R_f\mathcal{F}(g)(\omega) = \mathcal{F}(g)(\omega + f) = \int_{-\infty}^{+\infty} e^{-\mathrm{i}2\pi\omega y} \cdot b'(y) \cdot e^{\mathrm{i}\alpha(y)} \, \mathrm{d}y \tag{4.3}$$

The rotation by R_f shifts the peak at frequency f to zero. This eliminates the $2\pi fy$ phase factor.

- **Inverse Fourier Transformation**

$$\mathcal{F}^{-1}(R_f\mathcal{F}(g))(y) = b'(y) \cdot e^{\mathrm{i}\alpha(y)} =: A(y) \tag{4.4}$$

A contains the information about the phase shift α as well as remaining effects of b denoted by b'. These are minor effects due to imperfection at mirrors, lenses and polarizers or inhomogeneities of the two windows the laser passes through. These effects are eliminated by the next step.

- $\mathbf{A/A_{ref}}$ (point–wise)
Divide A by A_{ref} which is the signal obtained by the same transformation applied to the reference data without gas jet. The phase of the remaining term corresponds to the phase caused by the gas jet.

The term $e^{\mathrm{i}2\pi fy}$ would arise as well in A_{ref} and therefore is cancelled in the last step, even if the rotation R_f is omitted. As explained in section 2.1 the Wollaston Interferometer measures phase difference between rays separated by a distance d in the object plane. Therefore, phase shifts obtained at two points in the image plane that are separated by a distance corresponding to d have to be added up. The ideas behind the routine explained above come from the PhD thesis of Gilliss McNaughton Dyer [12]. The corresponding Python functions can be found in the appendix 8.4. The procedure yields the phase ϕ which a ray has picked up when passing through the gas jet.

$$\phi(y) = \frac{2\pi}{\lambda} \int (n(y,z) - 1) \, \mathrm{d}z, \tag{4.5}$$

where the integration path goes along the ray at position y, λ is the wavelength of the laser and n refers to the refractive index of the gas distribution. Once cylindrical symmetry of the gas distribution is assumed, obtaining the radial density distribution $\rho(r)$ from $\phi(y)$ is possible. The corresponding integral relation is called inverse Abel transformation and is explained in the next section.

4.2 Abel Inversion

The phase shift ϕ, extracted with the method explained before, is proportional to a projection of the gas jet along the propagation direction of the laser. Here, cylindrical symmetry of the gas distribution is assumed. This assumption enables to reconstruct the radial density distribution from ϕ. This is achieved by the inverse Abel transform. The Abel transform is nicely explained in [13] or [14], and reads:

$$\phi(y) = \frac{\Delta s}{\lambda} 2\pi = \frac{2\pi}{\lambda} 2 \int_0^\infty (n(y,z) - 1) \mathrm{d}z = \frac{4\pi}{\lambda} \int_y^\infty (n(r) - 1) \frac{r}{\sqrt{r^2 - y^2}} \mathrm{d}r \tag{4.6}$$

$$F(y) := \frac{\phi(y)\lambda}{2\pi} = 2 \int_y^\infty (n(r) - 1) \frac{r}{\sqrt{r^2 - y^2}} \mathrm{d}r \tag{4.7}$$

$$\overset{\text{inv. Abel}}{\Longrightarrow} (n(r) - 1) = -\frac{1}{\pi} \int_r^\infty \frac{\mathrm{d}F(y)}{\mathrm{d}y} \frac{\mathrm{d}y}{\sqrt{y^2 - r^2}}. \tag{4.8}$$

The derivative and the integral occurring in equation 4.8 are calculated with the routines exposed by Joshua Stults [15]. The key points are summarised here. It is not suitable to approximate the derivative of F by the discrete differential quotient due to noise, since this would amplify noise drastically. A more sophisticated method based on Gaussian filters is needed. Consider the following Fourier identity for f, g functions with compact support. All integrals appearing in equations 4.9 - 4.13 are defined on the interval from $-\infty$ to $+\infty$.

$$F(f) \cdot \mathcal{F}\left(\frac{\mathrm{d}g}{dx}\right) = \int \mathrm{d}x \; e^{-\mathrm{i}2\pi x\omega} f(x) \cdot \int \mathrm{d}x \; e^{-\mathrm{i}2\pi x\omega} \frac{\mathrm{d}g(x)}{dx} \tag{4.9}$$

$$= \int \mathrm{d}x \; e^{-\mathrm{i}2\pi x\omega} f(x) \cdot \int \mathrm{d}x \; e^{-\mathrm{i}2\pi x\omega} \; (\mathrm{i}2\pi\omega) \; g(x) \tag{4.10}$$

$$= \int \mathrm{d}x \; e^{-\mathrm{i}2\pi x\omega} \; (\mathrm{i}2\pi\omega) \; f(x) \cdot \int \mathrm{d}x \; e^{-\mathrm{i}2\pi x\omega} g(x) \tag{4.11}$$

$$= \int \mathrm{d}x \; e^{-\mathrm{i}2\pi x\omega} \frac{\mathrm{d}f(x)}{dx} \cdot \int \mathrm{d}x \; e^{-\mathrm{i}2\pi x\omega} g(x) \tag{4.12}$$

$$= F\left(\frac{\mathrm{d}f}{dx}\right) \cdot \mathcal{F}(g) \tag{4.13}$$

When g is set to a Gaussian distribution, rearranging this identity yields the smoothed derivative of a noisy signal f by using only the derivative of g instead of f (equation 4.9). The derivative of the Gaussian g can be easily evaluated from its analytical expression. Another issue is the singularity inside the integral of equation 4.8, when the integral is approximated on a discrete domain. This is solved by setting the first value of the integral ($y = r$) to the second value ($y = r + \Delta y$). For the limit of many points (i.e. infinitesimal grid spacing Δy) the numerical value of the integral will converge to the analytical value [15]. The Python function performing these calculations can be found in the appendix of my semester thesis [16] or on the hard disk drive of this thesis in the file `routines.py`.

4.3 Tomographic Reconstruction

The goal of tomographic reconstruction algorithms is to estimate a 3D density distribution based on its measured projections along directions with different angles. If rotational symmetry can be assumed Abel inversion provides an analytic method to reconstruct the 3D density distribution from a single projection, see section 4.2. Problems where rotational symmetry cannot be assumed demand for another reconstruction method. These kind of problems arise frequently in medical physics when a density image of tissue is desired, but only projections from x–ray scans or PET (positron emission tomography) data is available. A efficient algorithm is the so called Back Projection. As computation power increased drastically, more sophisticated algorithms were developed. One of these is the Maximum Likelihood – Expectation Maximization (ML–EM) algorithm [17], which is an iterative method with good convergence properties compared to Back Projection but, on the other hand, has a higher computational cost. In the following sections, both Back Projection and ML–EM are proposed and their advantages are discussed.

4.3.1 Back Projection

The idea of a simple Back Projection is to redistribute (back–project) the measured projections homogeneously along the projection lines. This procedure can be implemented efficiently but it can only provide rough information about the distribution. The reconstructed images become blurred, albeit infinite projections are available [17]. This behavior is studied with a generic non–symmetric distribution as shown in Figure 4.1. Due to the significant blurring in this example it is deduced that Back Projection is not suitable for reconstructing a sharp shock front in a gas jet.

4.3.2 Maximum Likelihood – Expectation Maximisation (ML–EM)

The basic principle of this algorithm is to advance an initial guess of the distribution iteratively by comparing the forward–projected data of the current guess with the measured data from all angles. The n–th estimate of the i–th voxel is named x_i^n. Often, the initial guess x_i^0 is chosen a homogeneous distribution. The ML–EM step that advances the guess is computed by the following equation [17]:

$$x_i^{n+1} = x_i^n \frac{1}{\sum_j A_{ij}} \sum_j A_{ij} R_j^n, \tag{4.14}$$

where R_j^n is the ratio of the value of measurement pixel y_j and the forward projected data of the n–th estimate:

$$R_j^n = \frac{y_j}{\sum_k A_{kj} x_k^n}. \tag{4.15}$$

The matrix A is the system matrix which accounts for how much each voxel contributes to each measurement. By this procedure, the advanced guess will approach a distribution that is compatible with all measurements. More precisely, the computed guess converges to a

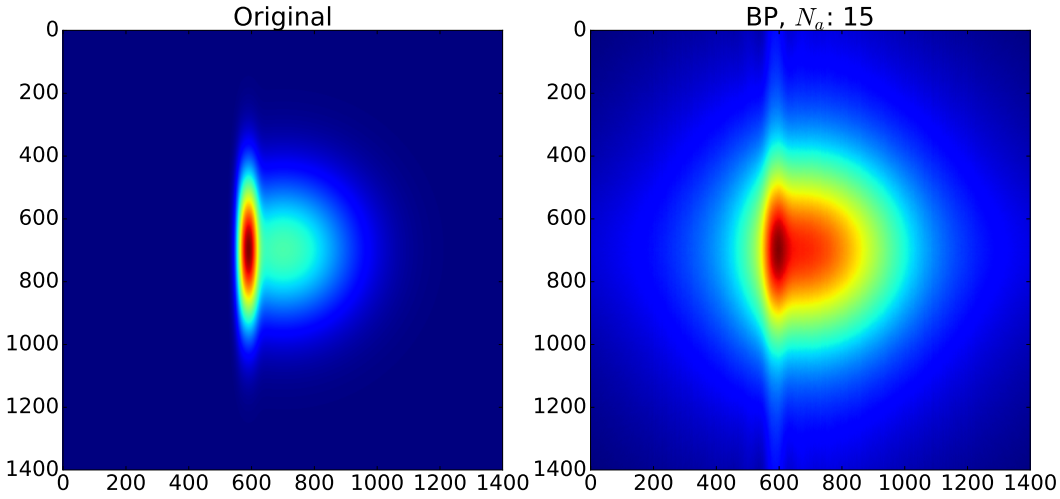

Figure 4.1: Illustration of the blurring effect of back projection. Number of projections from uniformly distributed angles $N_a = 15$. Gaussian noise ($\sigma = 0.01$) is added to the projection data before calculating the back projection.

distribution that has a high probability (maximum likelihood) to be the original distribution, given the measured data. The ideas of the algorithm are sketched in Figure 4.2. The implementation of a single ML–EM step as a Python function can be found in the appendix 8.4. The full implementation as a loop can be found in the file `tomography2.py` on the hard disk drive of this thesis. To validate the algorithm several tests are performed. First, the ML–EM algorithm is run with a single phase projection from the undisturbed gas jet. The reconstructed radial density distribution agrees well with the result by Abel inversion (Figure 4.3). Abel inversion shows non–smooth behaviour around $r = 0$ due to the singularity explained in section 4.2. This problem does not arise with the ML–EM algorithm. To validate the performance of the algorithm on non–rotational symmetric distributions, it is tested on a known distribution. A 2D Gaussian multiplied by a step function is chosen, as the shock–wave by the razor blade is expected to have a similar shape. Figure 4.4 shows the generic distribution, as well as the reconstructed image from $N_a = 7$ projections after 15 iterations. Gaussian noise ($\sigma = 0.01$) is added to the projection data before running the ML–EM reconstruction. This figure shows that qualitative reconstruction of the original distribution without rotational symmetry is achieved. Numerical convergence properties of the ML–EM algorithm are studied under various conditions and are presented in the next section.

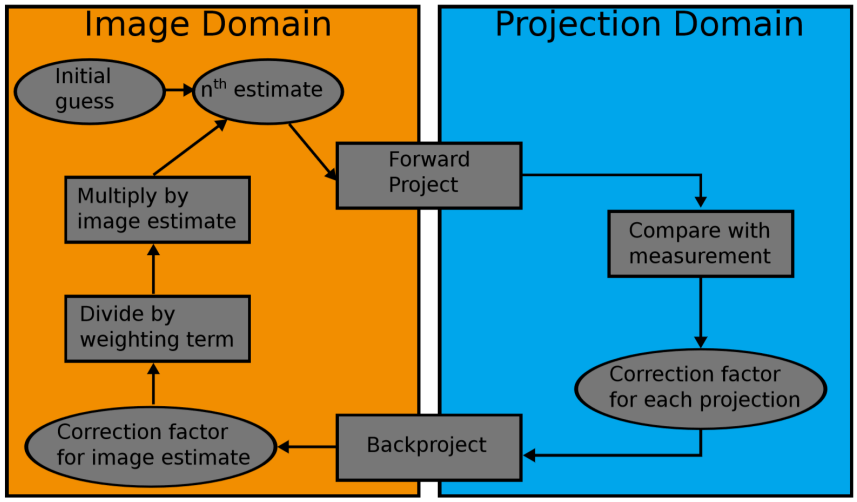

Figure 4.2: Scheme of Maximum Likelihood – Expectation Maximisazion (ML–EM) algorithm [17].

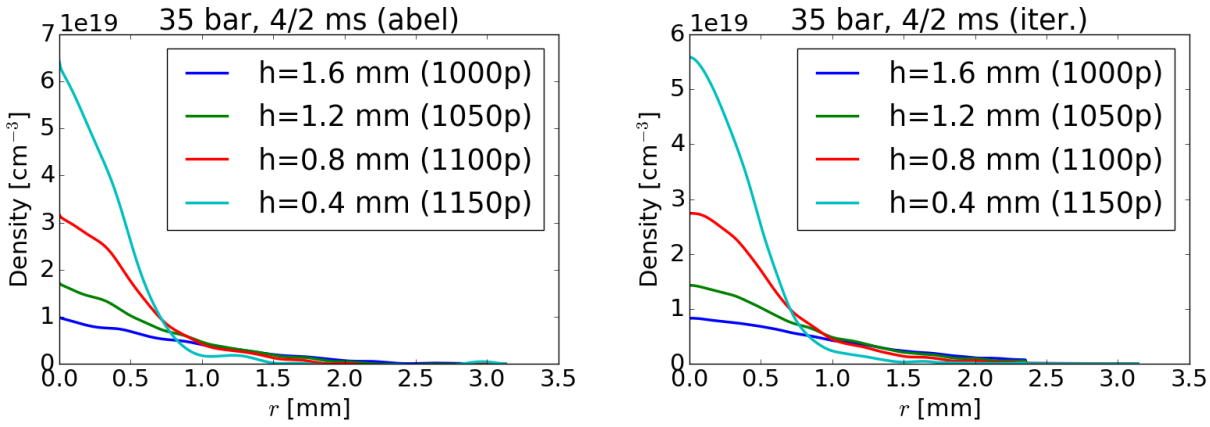

(a) Abel inversion

(b) ML–EM

Figure 4.3: Test of ML–EM on the undisturbed (rot.–symmetric) gas distribution. The distance from the nozzle is given in mm; the corresponding pixel row is placed in brackets. In general good agreement between Abel inversion (a) and ML–EM after 15 iterations (b). The problem due to the singularity of Abel inversion at $r = 0$ does not arise with ML–EM.

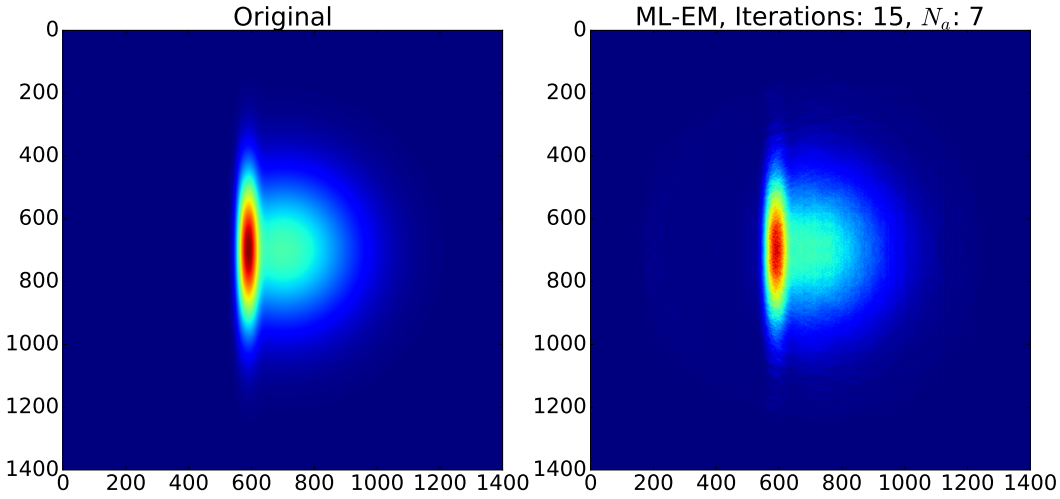

Figure 4.4: Example for reconstruction by ML–EM from 7 noisy projections, $\sigma = 0.01$.

4.3.3 Convergence and Error Studies of ML–EM

The convergence properties of the ML–EM algorithm are summarized in Figure 4.5, which shows the L_1 norm for the first 15 iterations for different numbers of measurements (number of projection angles N_a). Gaussian noise (standard deviation $\sigma = 0.01$-0.05) is added to the measurement. The reconstructed distribution matches the original distribution best if noise is lowest and, more interestingly, the error is not strongly correlated to the number of projections. The downside of many projection angles is that more noise is picked up. It turns out, that N_a around 7 achieves best convergence properties for the studied distribution and a noise level of $\sigma = 0.01$.

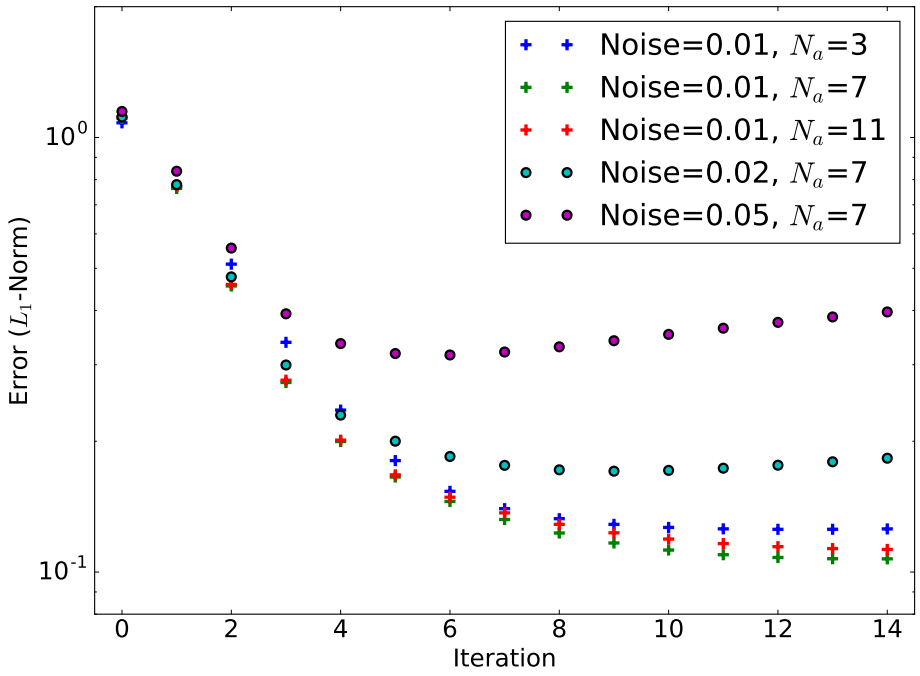

Figure 4.5: Convergence studies of ML–EM for varied Gaussian noise σ and number of projection angles N_a. Convergence is observed after 7-10 iterations.

Chapter 5

Density Measurements

Density measurements of gas jets operating with an arbitrary gas species can be carried out with the Wollaston interferometer described in section 3.1. Depending on the refractive index and density of the gas, averaging over a large number is necessary to increase the signal to noise ratio. The data processing is described in chapter 4. Non–rotational symmetric distributions can be evaluated via tomography. In this work two different gas jets (piezo and solenoid valves) with Argon are studied under various conditions. A shock front arising from a razor blade inserted to the gas flow of the solenoid jet is evaluated via tomography. In the following sections the measurement results of these scenarios are summarized.

5.1 Piezo Valve

The tunnel ionization monitor planned to measure the compression of the electron bunches in the free electron laser at PSI (SwissFEL) makes use of a piezo gas jet (Amsterdam Piezo-valve). This valve features short opening times down to 7 µs (300 times shorter than high speed solenoid valves by Parker), which helps to keep the gas load in the vacuum system low [18]. A disadvantage of piezo valves is that the valve closing mechanism can only sustain backing pressure up to 10 bar. Therefore, such valves are not suitable for high density applications. The interaction point of the electron bunch and the gas flow used in the tunnel ionization monitor at SwissFEL is 30 mm away from the nozzle. In order to measure the gas density up to the relevant distance the piezo valve is mounted to a linear vacuum stage. The opening time of the valve is set to 55 µs to measure the static gas flow without opening and closing effects of the valve (exposure time of CCD: 30 µs). Figure 5.1 shows the radial density distribution of the piezo valve for distances from 5 mm to 29 mm at 6 bar backing pressure. On the same figure, the full width at half maximum of the radial distribution is shown. The gas expands linearly with a half opening angle of 9° in the considered region. Figure 5.2 depicts the central density of the gas flow. After expanding over almost 30 mm the density is reduced by a factor of 20 down to $1.5 \times 10^{15}\,\mathrm{cm}^{-3}$. These measurements show good agreement with previous measurements of the piezo valve in the region closer to the valve (compare [16]).

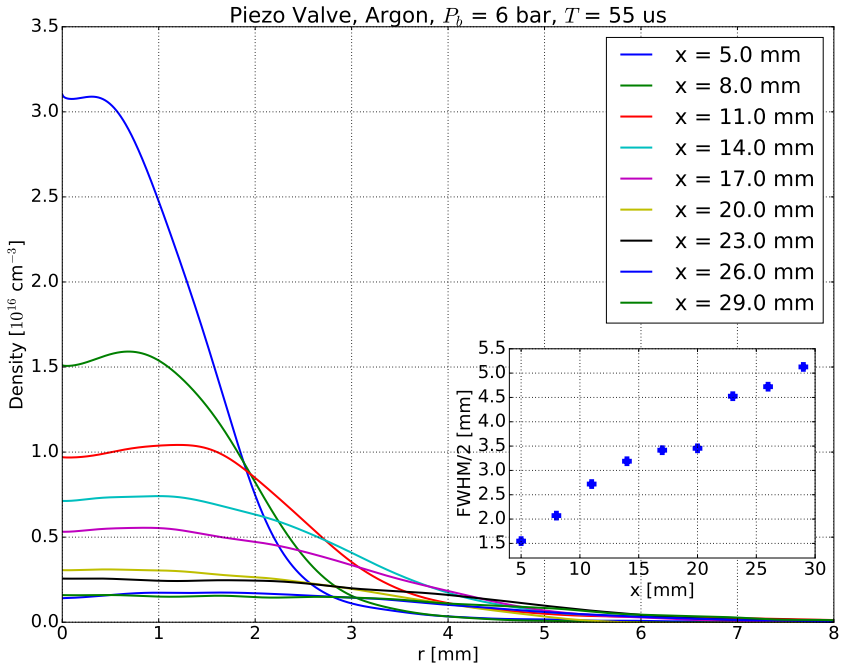

Figure 5.1: Long range (30 mm) density measurements of the piezo valve for the planned tunnel ionization monitor at SwissFEL. The reconstruction is computed via Abel inversion.

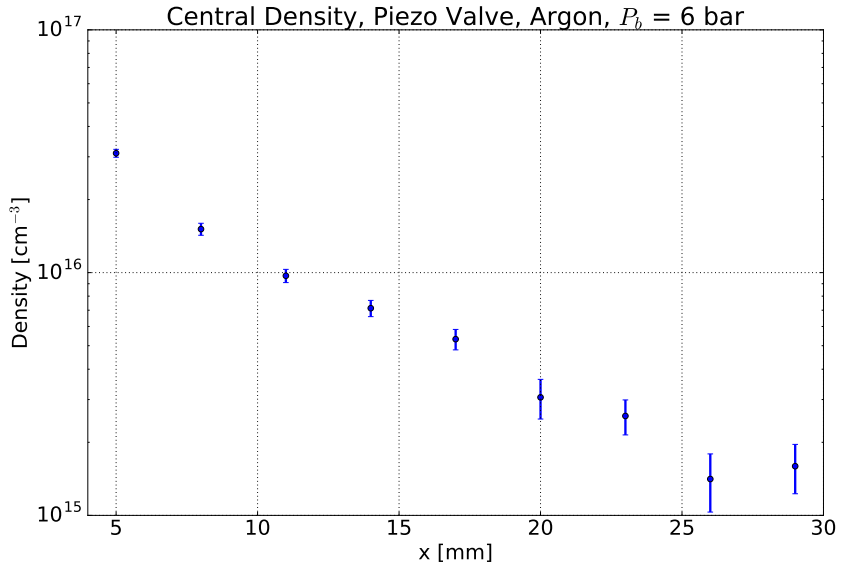

Figure 5.2: Central density reduces by factor of 20 after expanding for 25 mm.

5.2 Solenoid Valve

For the purpose of LWFA, Argon densities of one magnitude larger than the peak density, which the piezo valve can create, are needed. The Parker solenoid valve (Figure 3.3a) is expected to provide densities exceeding $1 \times 10^{18}\,\mathrm{cm}^{-3}$ at a distance of 2.6 mm from the nozzle, when operated with backing pressures around 35 bar (Figure 2.3). Due to geometric limitations (blade holder) the focused laser beam for LWFA cannot interact with the gas closer to the nozzle than 2.6 mm. The plasma frequency ω_p has to be matched with the laser pulse duration in order to excite the plasma wake resonantly. In the experiment the plasma frequency can be controlled by the Argon density and ultimately by the backing pressure applied to the valve. The central density measurement of the solenoid gas jet (without blade) for Argon is summarized in Figure 5.3. From this plot one can infer the required backing pressure to create the resonant electron density at a certain distance from the nozzle. For a laser pulse of length $\tau = 15\,\mathrm{fs}$ (FWHM) the required Argon density is $1.75 \times 10^{18}\,\mathrm{cm}^{-3}$, assuming the gas is ionized eight–fold (all valence electrons) [4]. Figure 5.3 also contains the density estimates from section 2.2. Good qualitative agreement between the model and the measurement is observed. But the measured densities are systematically higher than the estimate. A reason may be the fact that the estimate is based on the straight streamline model, which assumes that the expansion angle of the gas flow is equal to the opening angle of the nozzle [11]. But the measured expansion angle, defined by a linear fit to the FWHM of the gas distribution, is around 52° which is significantly smaller than the opening angle of the conical nozzle (90°). This would result in a higher particle density and could explain the discrepancy between the used model and the measurement results. Figure 5.3 (right) depicts the Argon density with respect to the backing pressure applied to the valve at fixed distances h. It is observed that the Argon density is increasing for backing pressures up to 37.5 bar. For even higher pressures the data indicates a stagnation and even a regression of the density. This can be explained by the working principle of the solenoid valve. When operating at higher backing pressures, a larger force is needed to lift the puppet out of the seal. Therefore, the valve may not open properly with too high backing pressures. This can result in a lowered density. To overcome the force of the backing pressure a high–voltage pulse (burst) is applied to the valve whose duration can be set internally. For the measurements shown here the burst duration is set to 220 µs. More information can be found in the appendix 8.2 and [19].

5.3 Shock Front Characterization

For the purpose of density down ramp injection in linear regime LWFA a razor blade is inserted laterally into the gas jet to create a supersonic shock front. A typical phase projection of the shock front is given in Figure 5.4. From the projection it can already be noted that the density gradient is decreasing with increasing distance from the nozzle. The tomographic data obtained with the rotational setup (Figure 3.4) is analysed via the ML–EM reconstruction algorithm explained in section 4.3.2. Figure 5.5 depicts the reconstructed

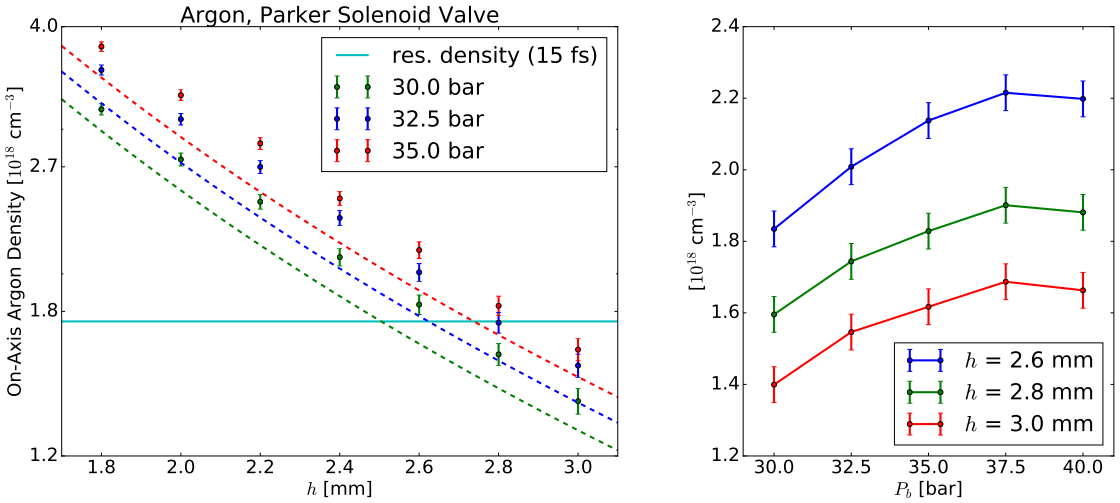

Figure 5.3: ML–EM reconstructed on–axis density of the solenoid valve without blade. Left: Dashed lines represent the estimate for the respective backing pressure. The resonant density is reached with backing pressures between 30 and 35 bar in the region of interaction for the Ti:Sa pulse ($h = 2.6 - 2.8$ mm). Right: The density appears to increase for pressures up to 37.5 bar. For higher pressures stagnation and even regression is observed.

density distribution of the shock front at 35 bar backing pressure. To study and optimize the ramp properties, this measurement is carried out for different backing pressures P_b and blade positions L_b from the center up to the edge of the gas flow (edge: $L_b = -3.2\,\text{mm}$). The ML–EM tomography is computed at several distances from the nozzle h. The range of these parameters is summarized in Table 5.1. The complete data set can be found in the folder `Tomography2` on the hard disk drive of this thesis. The files `tomography_view2.py` and `RampAnaPlots.py` provide tools to visualize the density distribution for parameters of interest (P_b, L_b, h, y). In order to evaluate the characteristics of the shock front numerically the following quantities are defined:

- Height h_s of the shock front: Density difference between ramped and undisturbed distribution at the ramp,
- Ramp factor r: Ramped peak density divided by undisturbed peak density,
- w_1: Half–width (left) defined by the ramp peak density,
- w_2: Half–width (right) defined by the height h_s.

For better understanding, the parameters w_1 and w_2 are indicated in Figure 5.6 which shows the density of a shock front as well as the undisturbed distribution along the z–direction. Main effect of the backing pressure is the central density which is plotted in Figure 5.3. The ramp characteristics are governed by the parameters L_b, h and y. Their respective effects are

Table 5.1: Parameters for shock front measurements.

	P_b [bar]	L_b [mm]	h [mm]	h [pixel]
min, max	30.0, 40.0	-3.2, -2.5	1.8, 3.0	1200, 1050
step	2.5	0.1	0.2	25

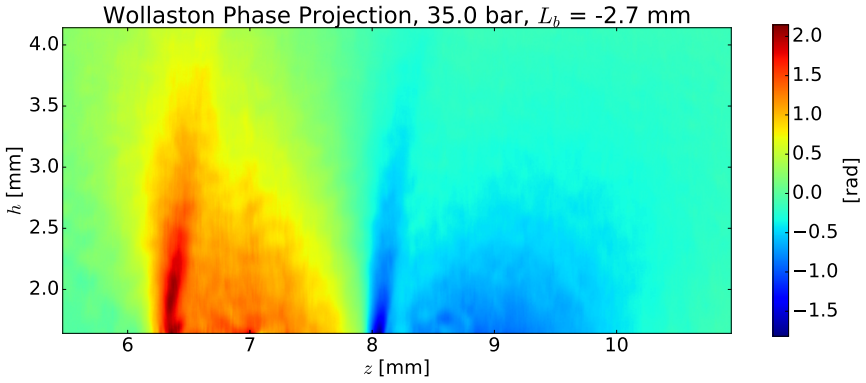

Figure 5.4: Typical Wollaston phase image of a shock front generated by a razor blade inserted from the left to a gas jet. Gas flow is directed upwards.

summarized in Figure 5.7 at a fixed backing pressure of 35 bar. A sharp density down–ramp is desirable to achieve a small electron energy spread in LWFA (see chapter 1). The length of the down–ramp is quantified by w_2 which is increasing with distance from the blade. A slight dependency of w_1 on the blade position L_b is observed with a local minimum at L_b = -2.8 mm. Another important quantity is the ramp factor r, which is mainly determined by L_b and y. It is larger when the blade is positioned closer to the center of the gas flow, as the ramp is created in a region of higher undisturbed density. The measurements indicate that the ramp factor also depends on the horizontal position y. In particular, r has a local maximum 0.5-0.6 mm displaced from the center. This is understandable by looking at profiles of a two dimensional Gaussian. When the profile is off–centered the distribution is flatter. This means that for a centered profile the density is rising more after the ramp, which results in a lower ramp factor.

5.4 Error and Stability Analysis

For the phase measurements of the piezo valve an average of 1000 images is taken in order to reduce noise. This leads to an error of below 1 mrad (standard deviation σ), which is needed in order to measure low densities down to $1.5 \times 10^{15}\,\mathrm{cm}^{-3}$ with an uncertainty

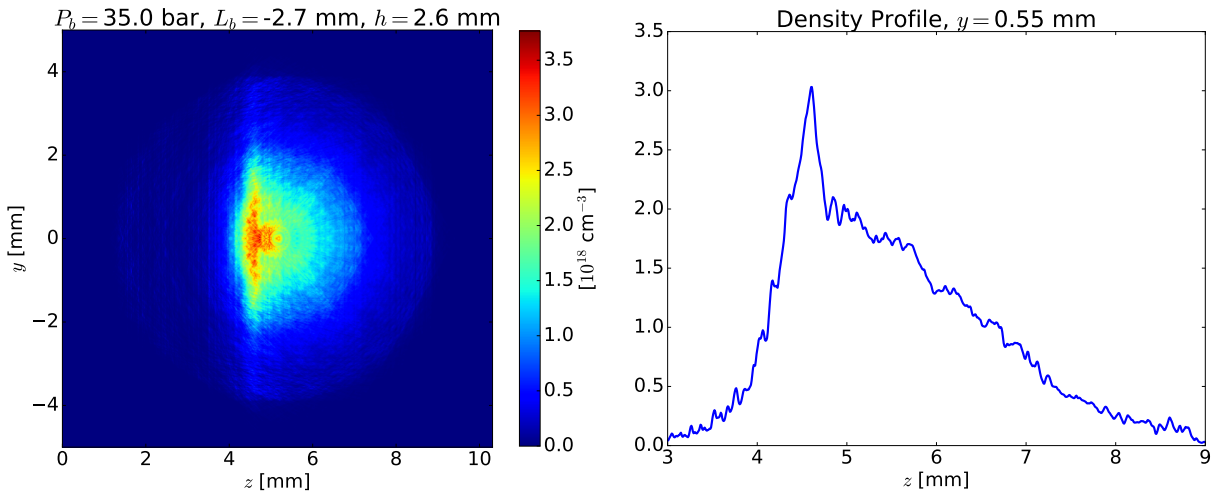

Figure 5.5: ML–EM reconstructed density distribution in a plane perpendicular to the gas flow at distance $h = 2.6\,\text{mm}$ from the nozzle, i.e. 1 mm from the blade.

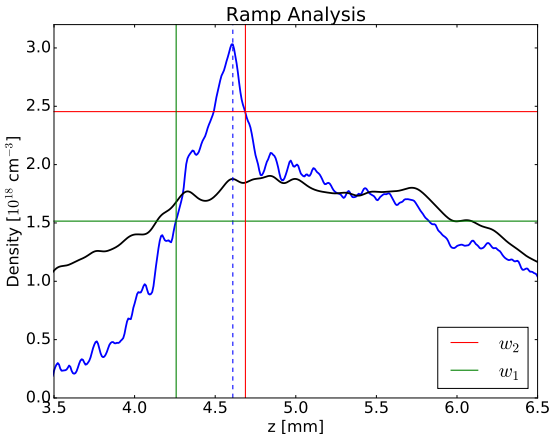

Figure 5.6: Example for ramp parameter analysis, undisturbed density in black.

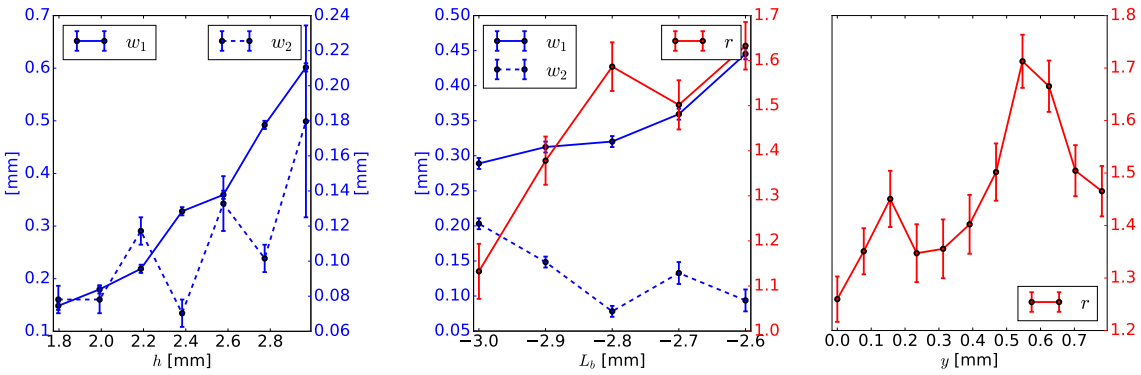

Figure 5.7: Ramp characterization with respect to h, L_b and y

of $0.4 \times 10^{15}\,\mathrm{cm}^{-3}$. Further information about the error analysis in this scenario can be found in my semester thesis [16]. In case of the solenoid valve, the purpose is to create and measure a shock front with densities up to 3 magnitudes larger than in the scenario described above. Combined with the fact that tomography requires more data (phase projections from different angles), it is decided to reduce the number of images per measurement drastically. The average of the phase projection is taken over 10 samples. The variation in peak phase of 10 samples is relatively small. For instance, the peak density in the shock front at 35 bar, 1 mm away from the nozzle is 1.5 rad and has a standard deviation of 0.05 rad. After averaging, the phase signal has noise in the order of 0.01 rad. As the maximum of the phase signal is around 1 rad, the ML–EM test (section 4.3.3) is realistic with a noise level of σ =0.01. (The generic distribution for this test is normalized, such that the maximum of the projections is equal to 1.) In agreement with the ML–EM convergence test, the number of iterations for the 3D density reconstruction is set to 10. Figure 5.8 shows the density distribution of the shock front at 35 bar after 10 iterations and the noise of the reconstructed image. The noise is calculated as follows. The data is fitted with a Savitzgy–Golay filter (window size: 51 pixel, polynomial order: 3). The fit is subtracted from the noise data, then divided into segments of 30 pixel (0.2 mm), over which the standard deviation is calculated. This provides a local error estimate of the reconstructed density. The noise ($\sigma < 1.4 \times 10^{17}\,\mathrm{cm}^{-3}$) in the region of the shock front is a factor of 20 lower than the peak density $2.8 \times 10^{18}\,\mathrm{cm}^{-3}$, i. e. the density change in the shock front is reconstructed with sufficient precision.

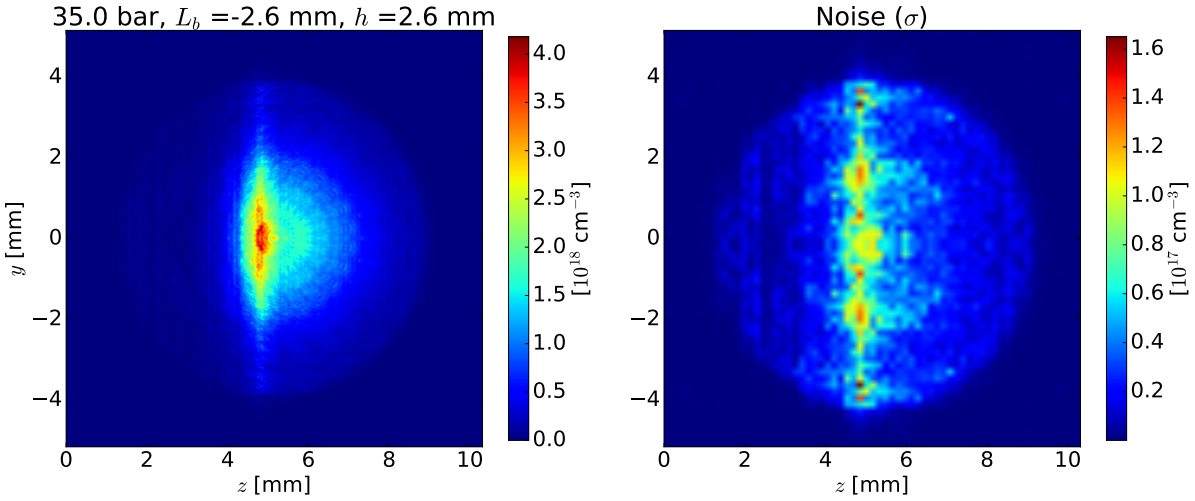

Figure 5.8: Error analysis of the reconstructed density (ML–EM, 15 iterations).

Chapter 6

Laser Wakefield Acceleration

For the second part of this thesis the interferometer and gas jet setup are moved to the Aramis Seedlaser at PSI. The goal is to demonstrate that LWFA is possible with this existing Ti:Sa laser facility which provides a 35 mJ pulse with a central wavelength of 800 nm at a repetition rate of 100 Hertz. The pulse length is controlled by the position of the gratings of the compressor. It is minimized experimentally on the sound intensity of the plasma created in air. This also corrects the dispersion in the vacuum window. We assume that a pulse length of 20 fs to 30 fs is achieved in this way. Previous density measurements have shown that three dimensional positioning of the laser focus with respect to the gas jet is needed to optimize the properties of the density ramp. As a first step, it is decided to measure only the charge of the created electron bunch via a Faraday cup. We expect to observe a correlation between the Argon density and the total accelerated charge. Particle–in–cell simulations with an open–source code (WARP: `http://warp.lbl.gov`) have shown that the properties of the electron bunch depend on the density (i. e. the plasma frequency with respect to the laser pulse length) and also on the ramp properties [4]. Depending on the ramp characteristics, only a small fraction of the electrons are injected into the wake and get accelerated. Using the Faraday cup measurement it is not possible to separate these electrons from the background (electrons leaving the wake before getting trapped). Effects concerning injection will be examined by analysing the electron bunch with an energy spectrometer.

6.1 Setup for Focusing and Positioning the Ti:Sa Laser

The experimental setup for guiding and focusing the Ti:Sa laser pulse (800 nm, 35 mJ) is integrated to the interferometry setup described in section 3.1, with the advantage that the Argon density can be observed in parallel. The full setup is sketched in Figure 6.1. Since the vacuum chamber containing the gas jet is heavy (approx. 30 kg) and is connected to the vacuum pump via a pipe, it is decided to leave the gas jet at a fixed position and move the focus of the laser relative to it. In order to achieve 3D positioning, the last three mirrors of the Ti:Sa setup are mounted on linear translation stages (Thorlabs, PT1–Z8) as depicted in Figure 6.1. The last mirror is a 90° off–axis parabolic mirror (OAP) which focuses the beam

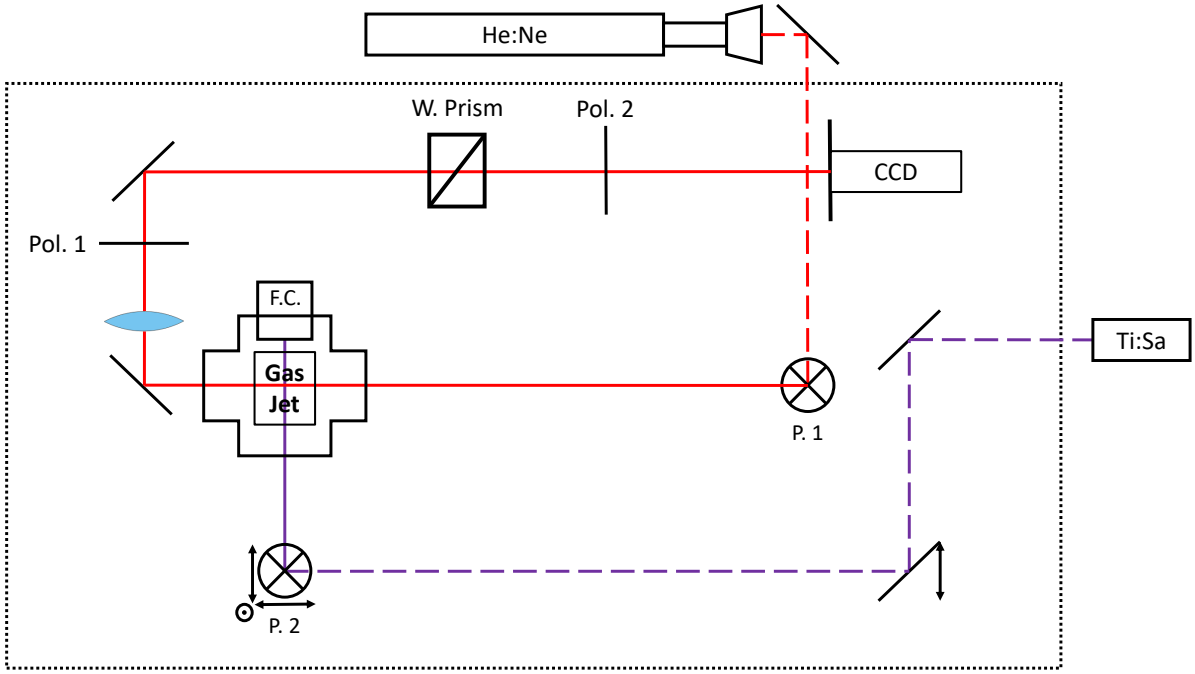

Figure 6.1: Combined setup for Interferometry (red) and LWFA with the Ti:Sa (purple). Dashed lines represent beams on table height; solid lines stand for beams at the height of the gas jet. The focusing off–axis parabola is part of the Ti:Sa periscope (P. 2). Mirrors on linear stages for focus positioning are indicated by arrows in the respective direction. A Faraday Cup (F.C.) for charge measurements is connected directly to the vacuum chamber.

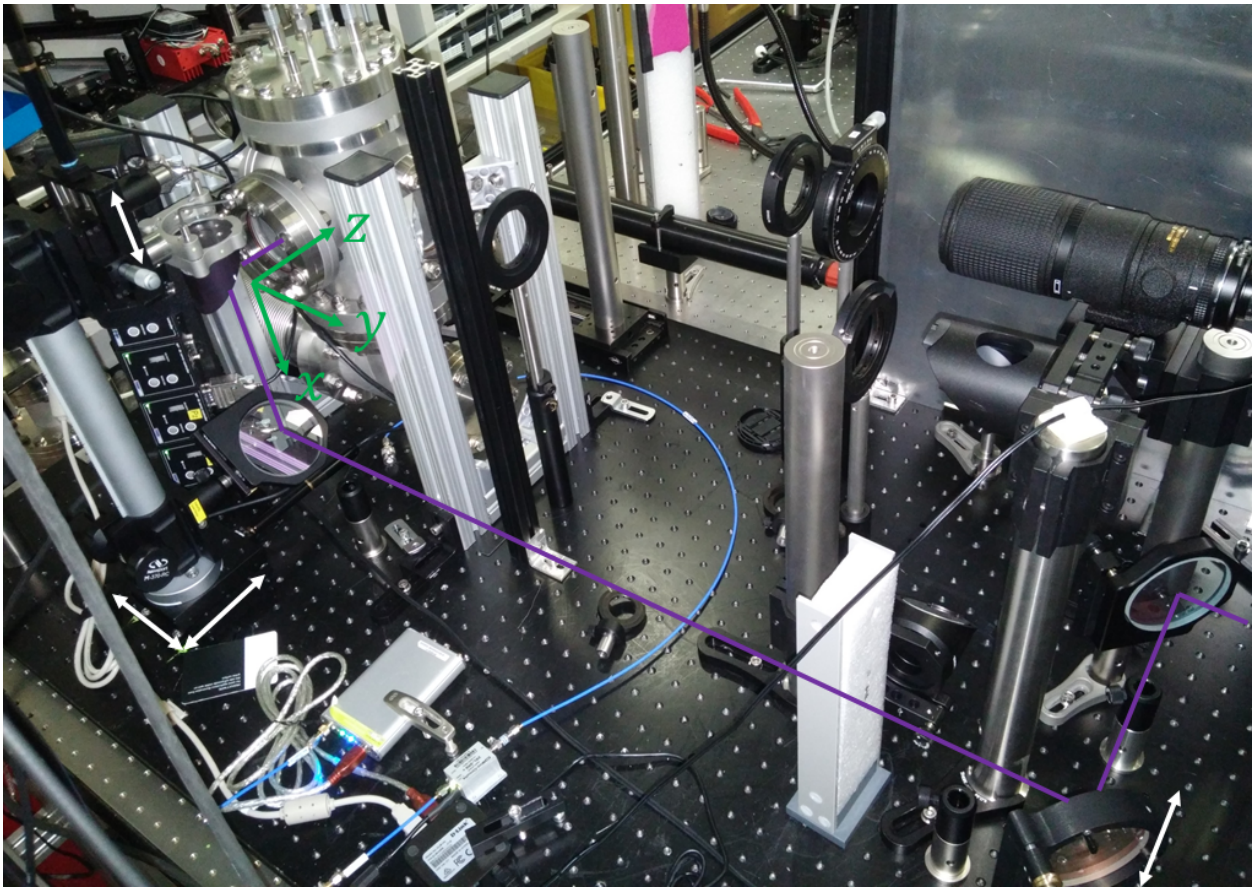

Figure 6.2: Combined experimental setup for Wollaston interferometry and LWFA. Ti:Sa laser indicated in purple.

through a vacuum window into the gas jet. The final two mirrors form a vertical periscope (Figure 6.2). For moving the focus along the direction of the gas flow (x) the OAP is moved up and down. For scanning along the horizontal direction (y) the complete periscope is moved. In order to keep the beam centered on the OAP when moving the periscope in z, the mirror in front of the periscope has to be moved accordingly. The used OAP (Thorlabs, MPD508762–90–M01) has a reflected focal length of 152.4 mm and a diameter of 50.8 mm. The reflectance of the OAP for wavelengths around 800 nm is above 95%. The dielectric mirrors (TLMB–800–45P–PW1, Melles Griot) feature a reflectance larger than 99.5% for wavelengths between 740 nm to 860 nm [20]. Therefore the total energy loss in the optical setup is assumed to be less than 2 mJ. The focal spot size is measured with a CMOS camera (Basler, ace acA3800–14gm) which features a pixel size of 1.67 µm. The CMOS sensor is positioned by a linear stage along z inside the vacuum chamber. A spot size of 5 µm to 6 µm (FWHM) is achieved when the OAP is aligned accurately (Figure 6.3). A two dimensional (x, y) focus position scan is displayed in Figure 6.4, which shows the FWHM contours of the foci for 100 positions on a grid with a spacing of 0.2 mm. The contour finding routine of the Python package scikit–image [21] is used to find the FWHM contour. During the position scanning the FWHM stays below 8 µm in both directions. When scanning long distances (>1 mm) in z the focus may not lie in the plane of the image sensor anymore due to imperfect alignment between the CMOS screen and the scanning stages. Scanning the focal point with the camera stage along z yields the original focus quality. The focal displacement after a 2 mm scan along z is around 50 µm, which corresponds to a misalignment of 25 mrad of the camera stage. This also shows, that the focus quality in this setup is not sensitive to the movements of the stages.

6.2 Faraday Cup

For the first test of the laser driven plasma accelerator it is decided to use a Faraday cup for charge measurements. A Faraday cup consists of a conducting damping block where charged particles are to be absorbed. Integrating the resulting current through a measurement circuit yields the deposited charge. The thickness of the absorbing block depends on the material and the expected energy of the incident particles. The range Δx of a particle in a material is defined by the stopping power $S(E)$ which is the energy loss per path length and which is a material dependent property.

$$\Delta x = \int_0^{E_0} \frac{1}{S(E)} \mathrm{d}E \tag{6.1}$$

Figure 6.5 depicts the stopping power as well as the range with respect to the particles initial energy for copper (Z=29) and aluminum (Z=13). Due to the higher atomic number of copper, the stopping power is substantially higher. According to WARP simulations of the LWFA process the maximum electron energy is below 20 MeV [4]. An electron with this energy will be absorbed in aluminum after approximately 3.7 cm, whereas in copper the particle will loose its energy within only 0.5 cm. In order to keep the size of the Faraday cup as small as possible, the absorber is chosen to be made of copper. The collector has

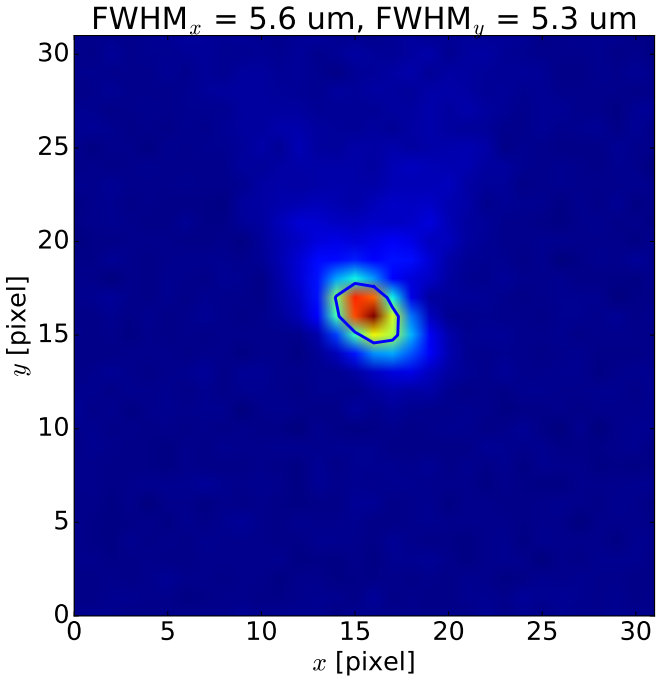

Figure 6.3: Focal spot size measurement with CMOS camera (Basler, ace acA3800–14gm).

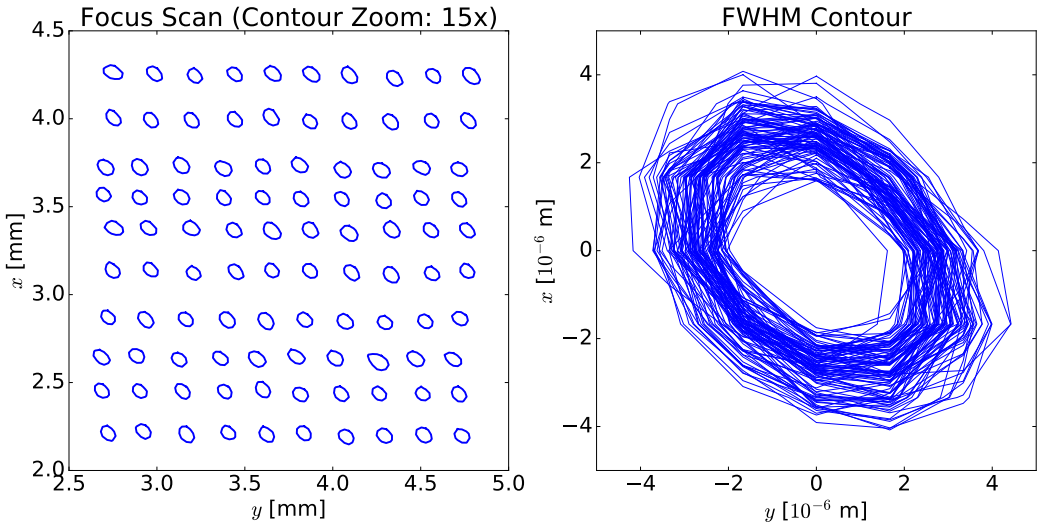

Figure 6.4: Left: 2D position scan of the focus in x and y. For visualization, the FWHM contours are magnified by a factor of 15. Right: The 100 contours of the scan plotted around their center. The FWHM stays below 8 µm for the entire scan.

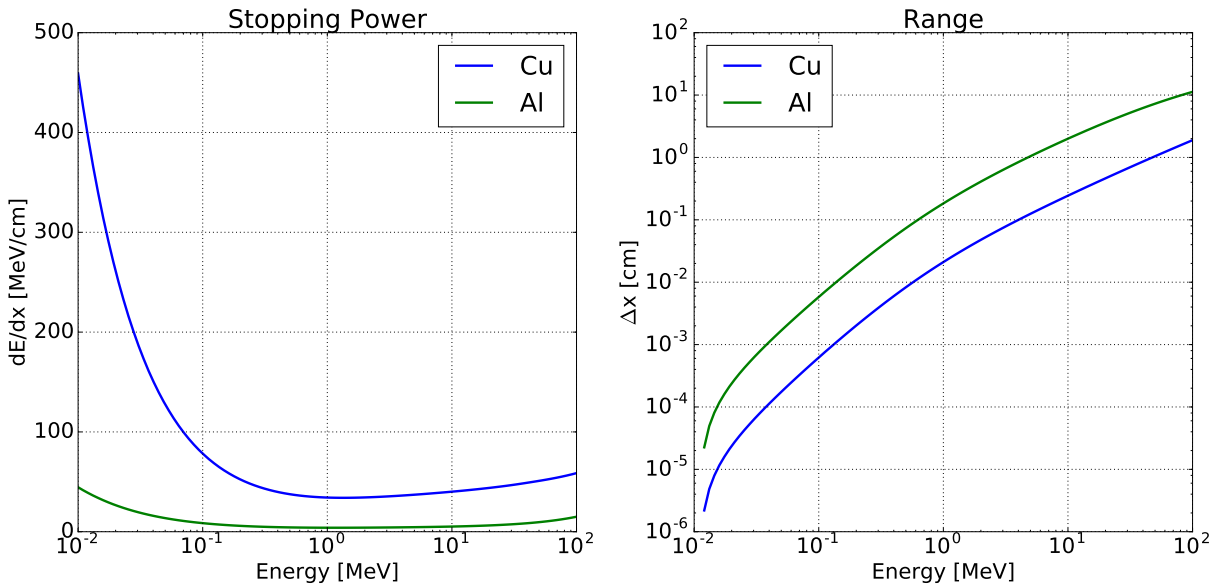

Figure 6.5: Stopping power $S(E)$ and range Δx of a particle with initial energy E. Data taken from the NIST ESTAR database [22].

a conical shape to reduce losses due to secondarily emitted electrons. To shield the charge signal from noise arising from the laser and the fields of plasma oscillations, the absorber is placed inside a grounded thin aluminum housing. The front, facing the electron beam, is covered by four layers of aluminum foil (total: 40 µm). Aluminum of this thickness blocks electrons with energies up to 75 keV. The CAD design and manufacturing of the charge detector were kindly done by Dominique Zehnder at PSI. Figure 6.6 shows the Faraday cup with the conical copper absorber. The CAD drawing can be found in appendix 8.3. The measurement circuit including the Faraday cup and the oscilloscope forms an RLC circuit. When reflections at the ends of the cables are neglected, the dynamics of the signal are modeled by the Kirchhoff rules, giving a second order differential equation:

$$\frac{\mathrm{d}^2 I}{\mathrm{d}t^2} + 2\delta \frac{\mathrm{d}I}{\mathrm{d}t} + \omega_0^2 I = 0. \tag{6.2}$$

In this equation, I is the electrical current, $\delta = R/(2L)$ is the damping constant, which depends on the resistance R and inductance L, and $\omega_0 = 1/\sqrt{LC}$ is the resonant frequency of the circuit, which depends on the inductance and the capacity C. The solution of equation 6.2 with the boundary conditions $I(0) = 0$ and $Q(0) = Q_0$ (initial charge deposited instantaneously) takes the form of a damped oscillator:

$$U(t) = RI(t) = -R\frac{\delta^2 + \omega_e^2}{\omega_e} Q_0 e^{-\delta t} \sin(\omega_e t), \tag{6.3}$$

with $\omega_e^2 = \omega_0^2 - \delta^2$. This model function is fitted with the `scipy.optimize.curve_fit` routine to the acquired signal in order to extract the deposited charge Q_0.

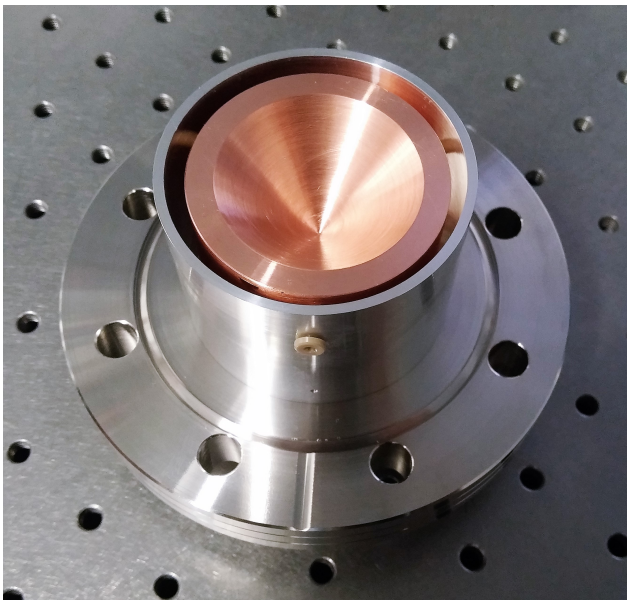

Figure 6.6: Faraday cup with conical copper absorber. For experiment the front is coverd by four layers of aluminum foil (40 µm) to block the laser and x–rays.

6.3 First LWFA Experiments

First LWFA experiments with the Ti:Sa Aramis Seedlaser and the optical setup described in section 6.1 were carried out in the last month of experimentation of this thesis. The charge is measured with a Faraday cup connected to an oscilloscope (WAVESURFER 44MXS–B, Teledyne LeCroy). The signal acquisition and gas jet are timed by a delay generator (DG645, Stanford Research Systems), which is triggered externally by a signal that is mode–locked to the laser. The Ti:Sa laser is running at 100 Hertz, whereas the gas jet is operated at 1 Hertz to reduce the gas load to the vacuum pump. A pre–trigger for the valve is not available. Therefore, the timing is set as follows. At time T_0 the delay generator is triggered by the first laser pulse (LP001). The gas jet is opened at $T_0 + 998\,\mathrm{ms}$ for 4 ms, i.e. the jet is opened during LP101. The read out of the Faraday cup is triggered with LP101 which also starts the next cycle. In every cycle LPx01 - LPx99 are unused. In principle, these pulses could be used for reference without gas. The focus is positioned in the center of the gas jet along the y direction by taking the camera for the focus scan as a reference. In the x-z plane the He:Ne interferometer is used for alignment. The heat created by the plasma in air is nicely observable. Using the 3D staging system (6.1) the focus is moved to the edge of the blade at a distance in x of approximately 1.0 mm to 1.3 mm from the blade. The resulting signal of the Faraday cup is amplified by a factor of 100 via a 10 dB attenuator (BW-S10W2+, Mini–Circuits) and a 30 dB amplifier (ZKL-2R5+, Mini–Circuits) to protect the oscilloscope from damage by a possible excess voltage. Figure 6.7 shows the measured data for different backing pressures P_b. A dependency of the signal on the backing pressure is clearly observable. Due to delays in cables and internal delays in the delay generator and

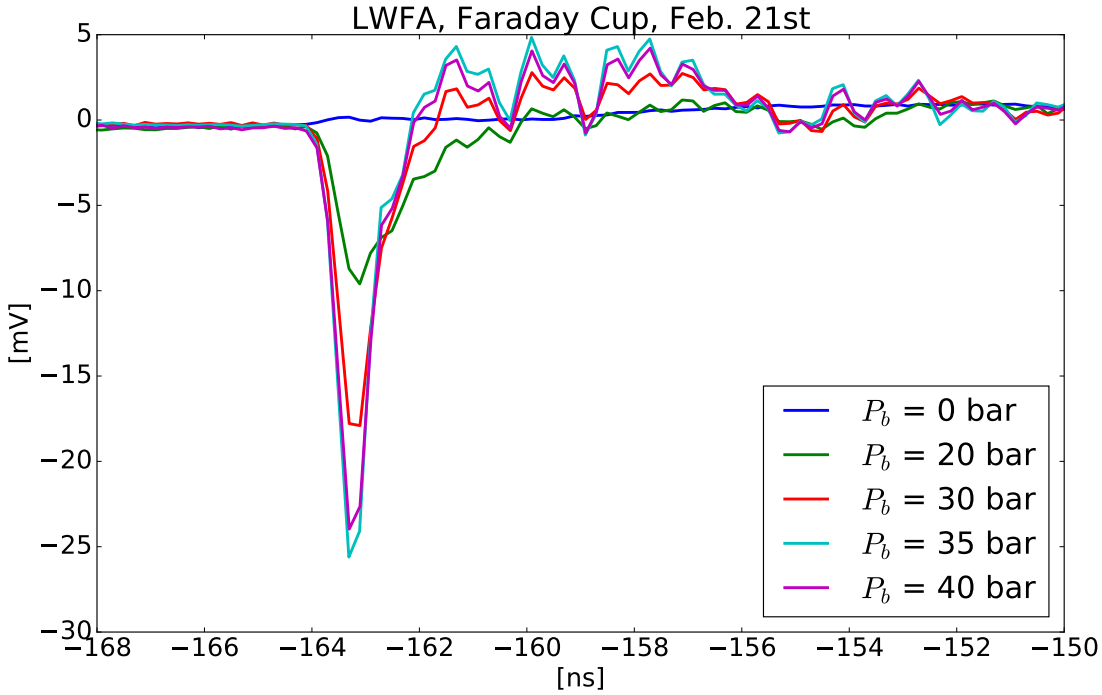

Figure 6.7: Faraday cup signal (100x amplification) for backing pressures from 0 to 40 bar.

the oscilloscope, the electron bunch arrives 164 ns before the data acquisition is triggered. Without gas, i.e. $P_b = 0$ the signal disappears. This confirms that the signal is not an effect of the laser itself, but due to the interaction of the laser with the gas. One effect that occurs when a focused infrared laser beam interacts with noble gases is high harmonic generation (HHG), where photons with energies up to 100 eV are generated [23]. Can these soft x–rays create free electrons via the photoelectric effect on the aluminum foil which hit the Faraday cup? A photon with an energy of 1 keV will penetrate 3.7 µm deep into aluminum [24]. Such a photon could then create an electron with an energy of at most 1keV. But, luckily, this electron will be absorbed within much less than 1 µm of aluminum (Figure 6.5). Four layers of aluminum foil covering the Faraday cup have a total thickness of 40 µm, which stops electrons with energies up to 75 keV (Figure 6.5). This would mean that electrons generated from HHG photons can certainly not reach the Faraday cup. This affirms that the Faraday cup signal is formed by electrons accelerated in the plasma. The charge of the electron bunch is obtained by fitting the acquired signal to the RLC model (equation 6.2). The results show a clear dependency on the backing pressure, which is of the same kind as the dependcy of the density on the backing pressure. Therefore, a strong correlation between the density of the gas jet and the measured charge (Figure 6.8a) is observed. To evaluate this correlation confidentially, more data with higher precision needs to be taken. Possibilities to achieve this are proposed in the following chapter.

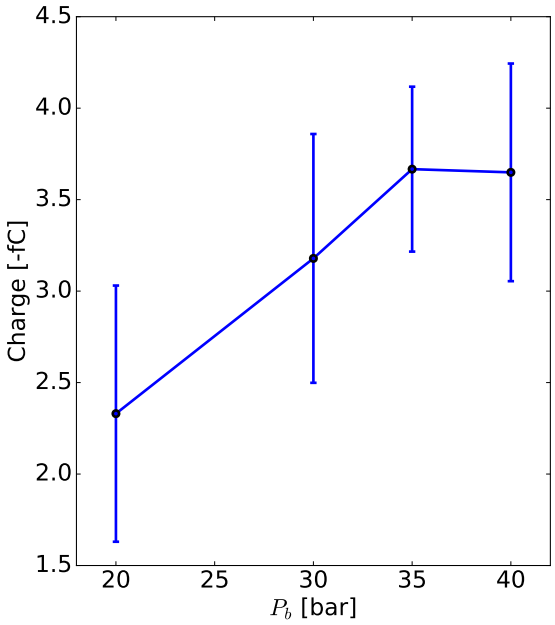

(a) Charge (from Faraday cup)

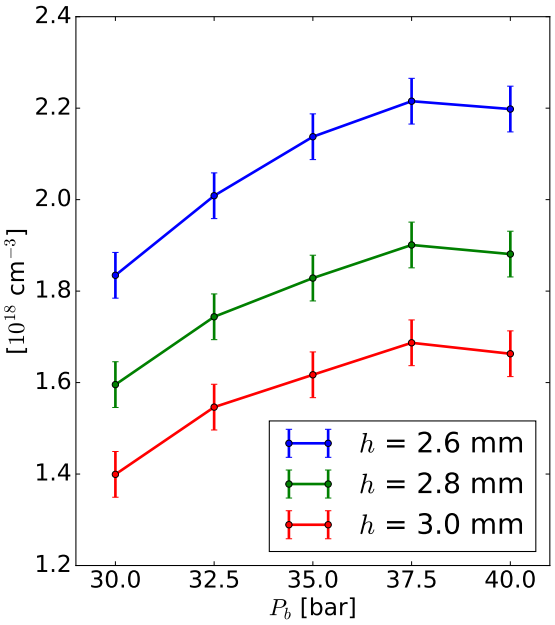

(b) ML–EM reconstructed on–axis density

Chapter 7

Summary and Outlook

Within the scope of the present master's thesis, gas jet studies with a single beam Wollaston interferometer were carried out for different purposes. A tunnel ionization monitor planned to measure the compression of the electron bunches in SwissFEL uses the ionizing effect of the electrons in a gas jet for peak current and bunch length measurements. In order to reduce the gas load in the vacuum system, a piezo gas jet, which enables short opening times of several µs is used here. Due to geometric limitations, the interaction point with the electron bunch is 3 cm away from the nozzle of the gas jet. A Wollaston prism interferometer is used to measure the density of the gas jet in the desired region. Abel inversion is used to reconstruct the density from a phase projection, as rotational symmetry can be assumed. After expanding over 3 cm, the density of Argon is around $1.5 \times 10^{15}\,\mathrm{cm}^{-3}$. Due to the low density, the data is averaged over 1000 measurements and an error of $0.4 \times 10^{15}\,\mathrm{cm}^{-3}$ is achieved in the region of interest.
Furthermore, the Wollaston interferometer is used to characterize a solenoid gas jet for the purpose of laser wakefield acceleration (LWFA) in the linear regime with the Aramis Seed-laser (Ti:Sa, 35 mJ) at PSI. The solenoid valve features much higher backing pressures (up to 80 bar) and can therefore provide higher Argon densities, which are needed to match the plasma frequency with the laser pulse length. A method to control the injection of electrons to the plasma wake is based on a density down ramp. This is successfully created with a razor blade inserted laterally to the gas jet, which creates a supersonic shock front at its edge. Due to the resulting asymmetrical gas distribution, tomographic reconstruction is needed to obtain the density from phase projections of different angles. Hence, a rotational setup for the razor blade is designed and a Maximum Likelihood – Expectation Maximization algorithm is developed, tested and applied to the data from the interferometer. A density drop by a factor of 1.8 within 100 µm at the interaction point with the laser (1 mm away from blade) is measured. A higher and sharper edge is created closer to the blade. Redesigning the holder for the blade would enable the use of larger density gradients for electron injection in LWFA, which would result in a lower energy spread of the accelerated bunch.
The first LWFA experiments with charge measurements via a Faraday cup were carried out during the last month of experimentation of this master's thesis. A strong correlation between the Argon density and accelerated charge (several fC) is observed. This experiment

is a first step towards a compact LWFA at PSI. The combination of an electron bunch with a femtosecond time structure and the possible repetition rate of 100 Hertz (Aramis Seedlaser) can lead to interesting applications in pump–probe experiments by ultra–fast electron diffraction. The repetition rate of the current setup is limited to a few Hertz by the vacuum system. This could be improved by attaching the turbo pump directly to the chamber.
For further investigation of the characteristics of the electron bunch and the injection effects due to the shock front, a more sophisticated analysis tool than the Faraday cup is needed. In order to measure the spatial distribution and the energy spread of the beam a spectrometer needs to be installed at the experiment. Nick Sauerwein has recently started his master's thesis with the goal of establishing a spectrometer unit including a magnetic quadrupole triplet for focusing and beam matching. This experiment can serve as a basis for students to gather first experience in the field of LWFA within the scope of the advanced physics laboratory at ETH Zurich or a summer school.
A first experiment concerning further acceleration of the extracted electron beam with a dielectric structure is in the planning stage (R. Ischebeck, ACHIP collaboration). The availability of three Ti:Sa beam lines in the Aramis Seedlaser facility will be extremely helpful for any kind of staging experiment in the future.

Chapter 8

Appendix

8.1 Assembly of Rotational Setup

The following pictures (8.1 to 8.5) are supposed to help assembling the rotational setup for tomography of the shock front created by a razor blade inserted to the solenoid gas jet.

8.2 IOTA ONE Solenoid Valve Controller

The solenoid valve by Parker used for the experiments of this master's thesis is controlled by a IOTA ONE driver which features continuous and pulsed mode. When the external cycle mode is activated an input TTL signal fully controls the opening and closing times of the valve. In the external single mode the valve is opened according to the rising edge of the input TTL, but the opening time is set explicitly on the front screen of the device. It is experimentally observed that the opening time should not be shorter than 2 ms to ensure complete opening of the valve. The IOTA ONE driver sends at the beginning of each opening a high–voltage (250 VDC to 300 VDC) burst, which is applied to the valve to reduce the reaction time of the system due to its inductance [19]. For backing pressures up to 35 bar a burst of 220 µs is sufficient. For all measurements shown in this thesis the burst is set to 220 µs. When using higher backing pressures, increase the burst length until consistent results are observed. Note: A longer burst will reduce the live time of the puppet holder [19].

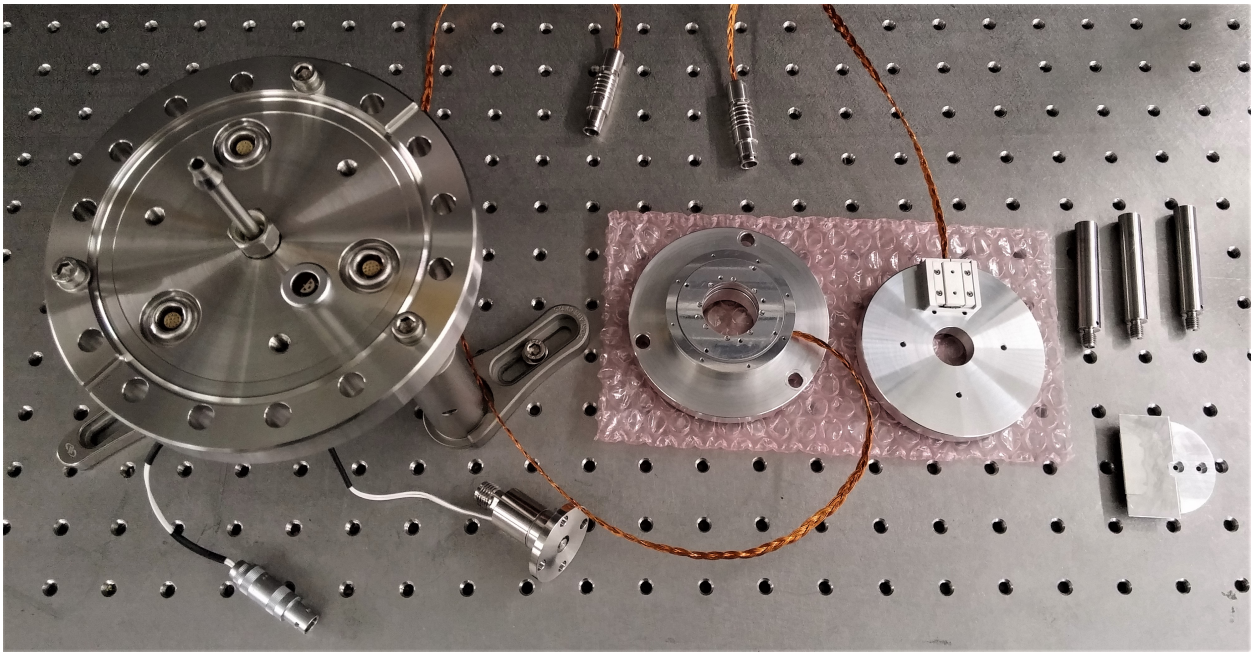

Figure 8.1: Components for tomography setup. DN CF 100 flange with feed–througs (gas, valve control, 3 Smaract stages), gas jet, rotational stage screwed to adapter plate 1, linear stage screwed to adapter plate 2, 3 custom posts, razor blade glued to aluminum holder.

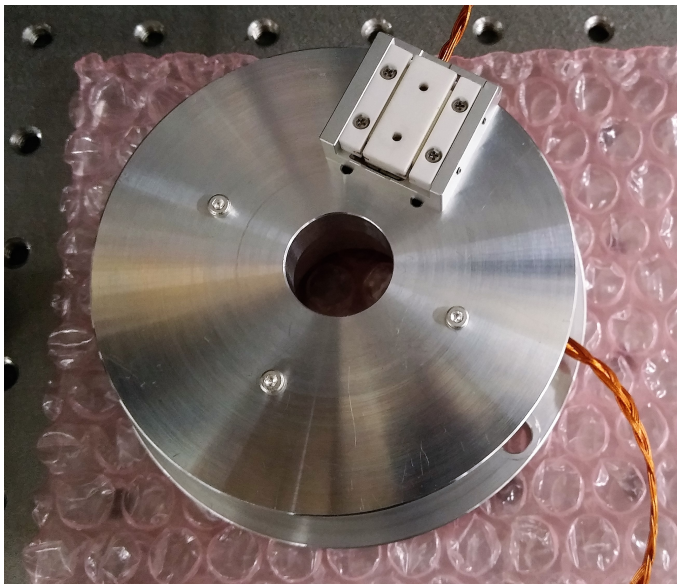

Figure 8.2: Connect adapter plate 2 (holding the linear stage) and the rotational stage with 3 M2 screws.

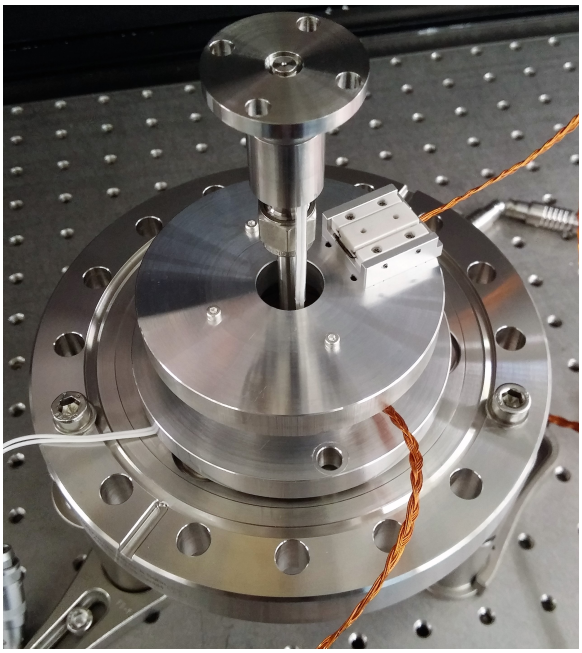

Figure 8.3: Place the positioner module (Figure 8.2) over the gas feed–through. Then, seal the gas jet to the feed–though with the Swagelok fitting, as depicted in the figure. Control the alignment of the jet. The Swagelok fitting is not accessible after the next step.

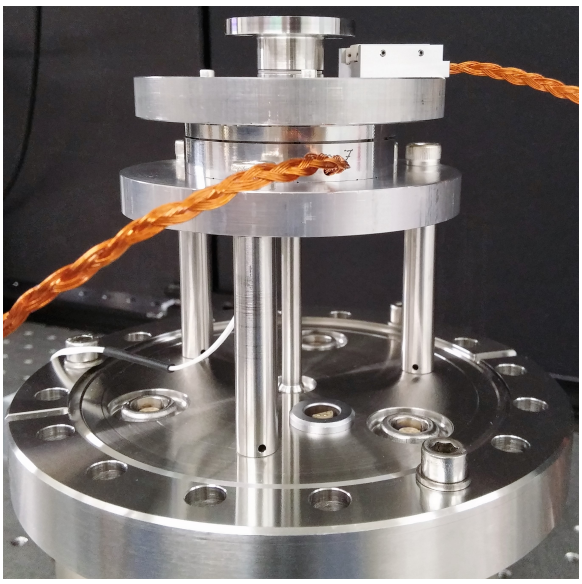

Figure 8.4: Lift the positioner module (Figure 8.2) up, so that the three posts (Figure 8.1) can be screwed onto the flange and to the positioner module with 3 M6 screws. Note: Unscrew adapter plate 2 in order to get better access to the M6 screws.

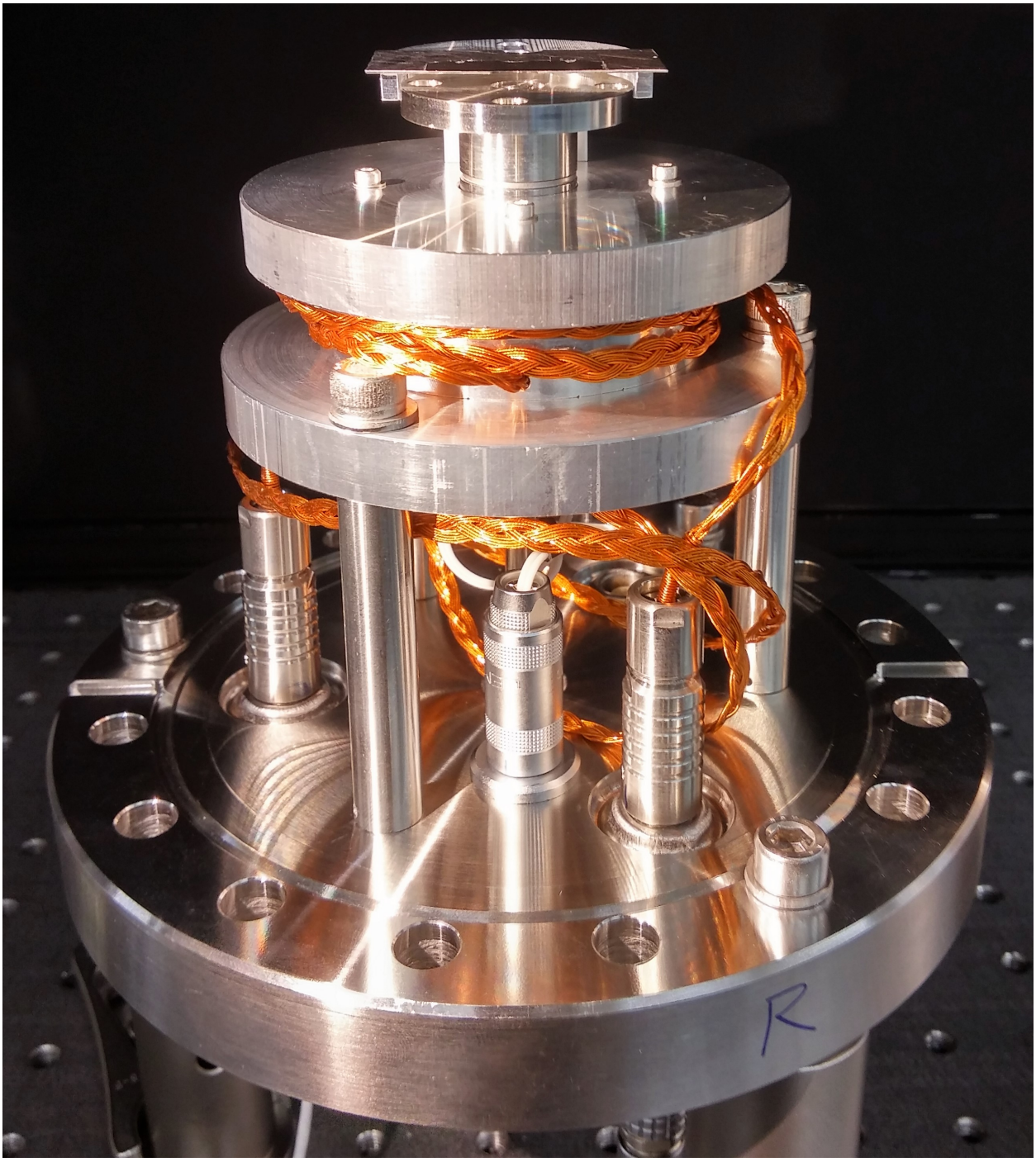

Figure 8.5: Mount the blade to the linear positioner with 2 M1.6 screws and connect the valve and stage control cables. Make sure, that the rotational stage can travel at least 180° without being blocked by the cable of the linear stage.

8.3 Faraday Cup Design

The design and manufacturing of the Faraday cup were kindly done by Dominique Zehnder (PSI).

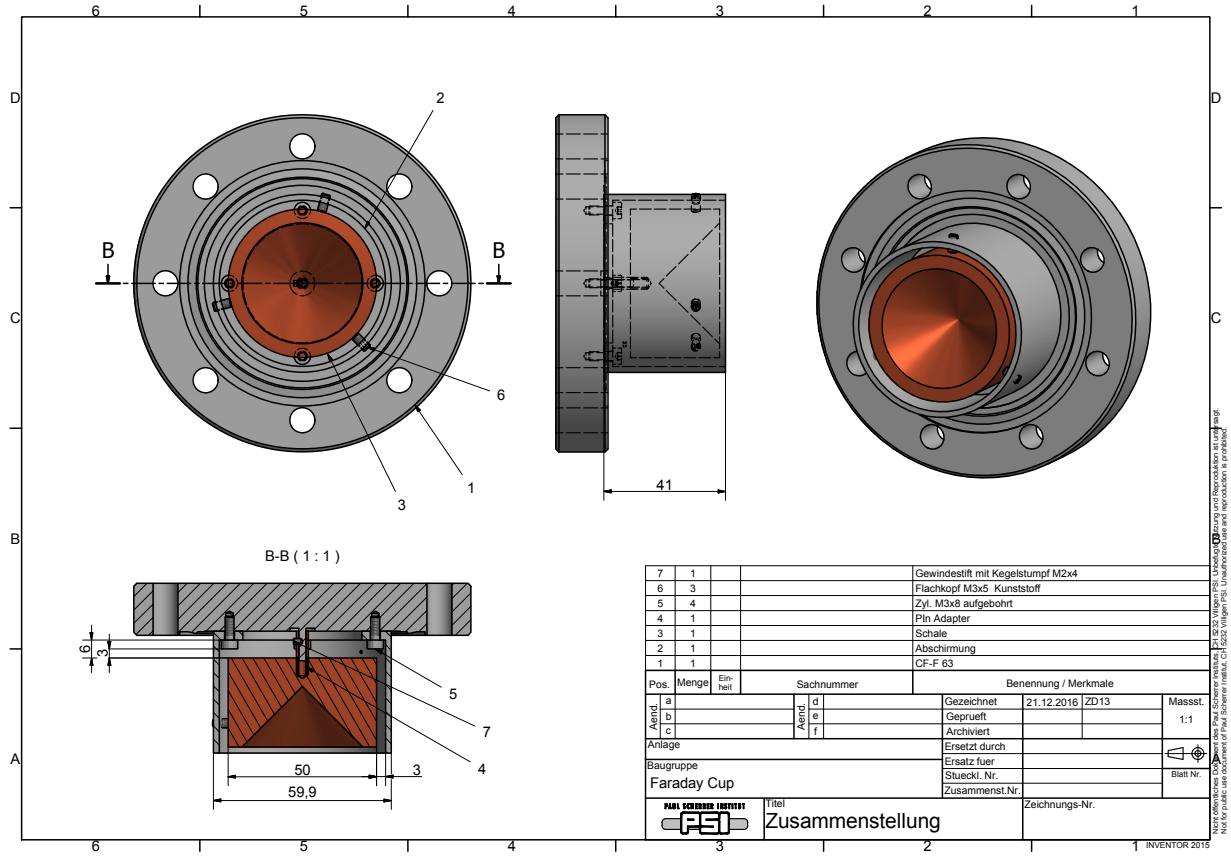

8.4 Python Functions

Interferometry Phase Unwrapping

```
import numpy as np

def GaussWindow(x):
    return np.exp(-1./x**2*(6.*(x[1]-x[0]))**2)

def FT(D):
    """
    Fourier Transformation
    """
    lx=len(D[:,0])
    kx = np.r_[-lx/2.:lx/2.]/lx
    F0=np.fft.fft(D,axis=0)
```

```
    F0=np.fft.fftshift(F0, axes=0)
    F0[lx/2:,:]=0.
    F0=np.transpose(np.transpose(F0)*GaussWindow(kx))
    IF0=np.fft.ifft(F0,axis=0)
    return IF0

def unwrap(D0,D1,fringe_dir='ver'):
    """
    Phase extraction
    fringe_dir: direction of undisturbed fringes.
    Depends on the orientiation of the W. prism.
    (standard: horizontal)
    """
    if fringe_dir=="hor":
        F0=FT(D0)
        F1=FT(D1)
    if fringe_dir=="ver":
        F0=FT(np.transpose(D0))
        F1=FT(np.transpose(D1))
    if fringe_dir=="hor": return np.angle(F1/F0)
    if fringe_dir=="ver": return np.transpose(np.angle(F1/F0))
```

ML–EM Step

```
from scipy import ndimage
import numpy as np

def MLEM(X,theta, meas):
    """
    One MLEM step for current guess X, angle theta,
    correspoding measurement data meas
    """
    Xp=ndimage.rotate(X, -theta, reshape=False)
    Lxt=len(X[0,:])
    X1=np.zeros((Lxt,Lxt))

    ysim=np.sum(Xp,axis=0)
    ZZ=(len(ysim)-len(meas))/2
    meas=np.append(ysim[:ZZ],meas)
    meas=np.append(meas,ysim[-ZZ:])

    R=np.abs(meas/ysim)
    X1[:,Lxt/4:-Lxt/4]=Xp[:,Lxt/4:-Lxt/4]*R[Lxt/4:-Lxt/4]

    return ndimage.rotate(X1,theta, reshape=False)
```

8.5 List of Main Devices

- Pulse Valve – Miniature High Speed High Vacuum Dispense Valve, 009–0442–900 . Parker, United States.
- Amsterdam Piezovalve (throat: 150 µm, opening angle: 20°). MassSpecpecD BV, The Netherlands.
- Piezo Controller EDU1. Electronica Beta–VU, The Netherlands.
- Vacuum Pump HiCube Eco 300. Pfeiffer, Germany.
- Wollaston Prism 30x30x5 mm, $\epsilon = 5.8$ mrad. Societe d'Optique de Precision Fichou, France.
- CCD Camera Interferometer, aviator avA2300–25gm. Basler, Germany.
- CCD Camera Microscope, scout scA1400–17gm. Basler, Germany.
- CMOS Camera Ti:Sa Focus, ace acA3800–14gm. Basler, Germany.
- AF Micro–Nikkor 200 mm f/4D IF–ED. Nikon, Japan.
- Oscilloscope Infiniium DSA80000B, 3 GHz, 40 GSa/s. Agilent, United States.
- Linear Vacuum Stage, SLC–1720–S. Smaract, Germany.
- Rotation Vacuum Stage, SR–5714C–S. Smaract, Germany.
- 90° Off–axis Parabolic Mirror, MPD508762–90–M01. Thorlabs, United States.
- 25 mm Motorized Translation Stage, PT1–Z8. Thorlabs, United States.
- Oscilloscope for Faraday Cup, WAVESURFER 44MXS–B. Teledyne LeCroy, United States.
- Dielectric Mirror for Ti:Sa, TLMB–800–45P–PW1. Melles Griot, IDEX Corporation, United States.

Acknowledgements

First of all, I wish to express my gratitude to Andreas Adelmann and Rasmus Ischebeck for the organization and motivating support during my entire time at PSI. I am indebted to Günther Dissertori for taking the initiative to make first contact with Andreas Adelmann enabling the whole project.
I am very thankful for the simulations carried out by Nick Sauerwein in advance of my thesis as well as his great help in the laser hutch for the first LWFA experiments towards the end of my thesis.
I wish to thank Christoph Hauri, Yunpei Deng, Christian Erny, Julien Réhault for providing the Ti:Sa laser for this experiment. I also wish to thank Peter Radi, Ivo Alxneit, Martin Beck, Franziska Frei, Martin Rohrer, Hanspeter Gehrig and Dominique Zehnder for their support concerning the experimental setup, especially for the construction of the Faraday cup by Dominique.
Finally, I am very grateful for the uncountably fruitful discussions about experimental, computational and mathematical issues with the fellow students Peter Zenz and Nick Sauerwein.

Bibliography

[1] S. M. Hooker. Developments in laser-driven plasma accelerators. *Nat Photon*, 7(10): 775–782, Oct 2013. ISSN 1749-4885. URL http://dx.doi.org/10.1038/nphoton.2013.234. Review.

[2] W. P. Leemans et al. Gev electron beams from a centimetre-scale accelerator. *Nat Phys*, 2(10):696–699, Oct 2006. ISSN 1745-2473. doi: 10.1038/nphys418. URL http://dx.doi.org/10.1038/nphys418.

[3] T. P. A. Ibbotson et al. Laser-wakefield acceleration of electron beams in a low density plasma channel. *Phys. Rev. ST Accel. Beams*, 13:031301, Mar 2010. doi: 10.1103/PhysRevSTAB.13.031301. URL https://link.aps.org/doi/10.1103/PhysRevSTAB.13.031301.

[4] N. Sauerwein. Design study for laser plasma wakefield acceleration of low energy electrons, 2016. ETH Zurich, Paul Scherrer Institute.

[5] C. Wang et al. Shock-wave-based density down ramp for electron injection. *Phys. Rev. ST Accel. Beams*, 15:020401, Feb 2012. doi: 10.1103/PhysRevSTAB.15.020401. URL http://link.aps.org/doi/10.1103/PhysRevSTAB.15.020401.

[6] R. Small et al. Single beam schlieren interferometer using a wollaston prism. *Appl. Opt.*, 11(4):858–862, Apr 1972. doi: 10.1364/AO.11.000858. URL http://ao.osa.org/abstract.cfm?URI=ao-11-4-858.

[7] M. Biss et al. Differential schlieren-interferometry with a simple adjustable wollaston-like prism. *Appl. Opt.*, 47(3):328–335, Jan 2008. doi: 10.1364/AO.47.000328. URL http://ao.osa.org/abstract.cfm?URI=ao-47-3-328.

[8] R. Benattar et al. Polarized light interferometer for laser fusion studies, 1979. URL http://scitation.aip.org/content/aip/journal/rsi/50/12/10.1063/1.1135764.

[9] W. Merzkirch. Generalized analysis of shearing interferometers as applied for gas dynamic studies. *Appl. Opt.*, 13(2):409–413, Feb 1974. doi: 10.1364/AO.13.000409. URL http://ao.osa.org/abstract.cfm?URI=ao-13-2-409.

[10] Y. Liu et al. Relationship of refractive index to mass density and self-consistency of mixing rules for multicomponent mixtures like ambient aerosols. *Journal of Aerosol Science*, 39(11):974986, 2008. doi: 10.1016/j.jaerosci.2008.06.006.

[11] C. Guanglong et al. Understanding of cluster size deviation by measuring the dimensions of cluster jet from conical nozzles. *AIP Advances*, 3(3):032133, 2013. doi: http://dx.doi.org/10.1063/1.4796187. URL `http://scitation.aip.org/content/aip/journal/adva/3/3/10.1063/1.4796187`.

[12] G. D. McNaughton. *Experimental Study of the Equation of State of Isochorically Heated Warm Dense Matter*. PhD thesis, The University of Texas at Austin, UMI: 3274779, 2007.

[13] S. Simons et al. The filtered abel transform and its application in combustion diagnostics. *NASA Technical Reports*, 2003. URL `http://ntrs.nasa.gov/search.jsp?R=20030031381`.

[14] "Wikipedia". Abel transform — wikipedia, the free encyclopedia, 2015. URL `https://en.wikipedia.org/w/index.php?title=Abel_transform&oldid=668868856`. [Online; accessed 20-May-2016].

[15] J. Stults. FFT-based abel inversion tutorial, Jan 2010. URL `http://www.variousconsequences.com/2010/01/fft-based-abel-inversion-tutorial.html`.

[16] B. Hermann. Schlieren interferometry of a pulsed gas jet, 2016. ETH Zurich, Paul Scherrer Institute.

[17] M. Zvolsky. Tomographic image reconstruction. An introduction., 2014. URL `http://www.desy.de/~garutti/LECTURES/BioMedical/Lecture7_ImageReconstruction.pdf`. DESY, University of Hamburg.

[18] D. Irimia et al. A short pulse (7 s fwhm) and high repetition rate (dc-5khz) cantilever piezovalve for pulsed atomic and molecular beams. *Review of Scientific Instruments*, 80(11):113303, 2009. doi: 10.1063/1.3263912. URL `http://dx.doi.org/10.1063/1.3263912`.

[19] *IOTA ONE Operating Manual and Setup Instructions*. Parker Hannifin Corporation, 2007.

[20] *Optics & Laser Catalog*. IDEX Optics & Photonics Marketplace, Albuquerque, NM, 2014. URL `http://www.optotec.co.jp/data/CVI_2014.pdf`.

[21] S. van der Walt et al. scikit-image: image processing in Python. *PeerJ*, 2:e453, 6 2014. ISSN 2167-8359. doi: 10.7717/peerj.453. URL `http://dx.doi.org/10.7717/peerj.453`.

[22] M. Berger et al. ESTAR, PSTAR, and ASTAR: Computer programs for calculating stopping-power and range tables for electrons, protons, and helium ions (version 1.2.3), 2005.

[23] A. Heinrich et al. Enhanced VUV-assisted high harmonic generation. *Journal of Physics B: Atomic, Molecular and Optical Physics*, 39(13):S275, 2006. URL `http://stacks.iop.org/0953-4075/39/i=13/a=S03`.

[24] J. Hubbell et al. Tables of x-ray mass attenuation coefficients and mass energy-absorption coefficients from 1 keV to 20 MeV for elements Z = 1 to 92 and 48 additional substances of dosimetric interest, 2004.